Quark-Antiquark Potentials from QCD and Quarkonium Spectroscopy

Alexander Laschka

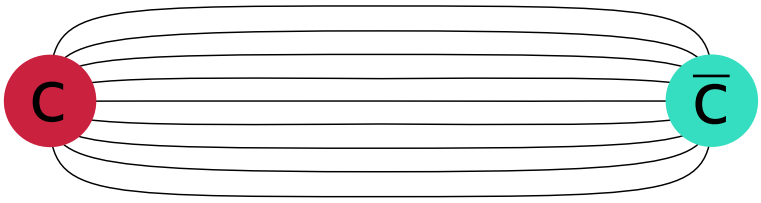

Technische Universität München

Technische Universität München
Institut für Theoretische Physik T39

Quark-Antiquark Potentials from QCD and Quarkonium Spectroscopy

Alexander Christian Laschka

Vollständiger Abdruck der von der Fakultät für Physik der Technischen Universität München zur Erlangung des akademisches Grades eines

Doktors der Naturwissenschaften (Dr. rer. nat.)

genehmigten Dissertation.

Vorsitzende:		Univ.-Prof. Dr. Laura Fabbietti
Prüfer der Dissertation:	1.	Univ.-Prof. Dr. Wolfram Weise (em.)
	2.	Univ.-Prof. Dr. Nora Brambilla

Die Dissertation wurde am 5. 12. 2012 bei der Technischen Universität München eingereicht und durch die Fakultät für Physik am 11. 12. 2012 angenommen.

Abstract

This work examines the interaction between a heavy quark and its antiquark. By combining perturbative and non-perturbative methods, interaction potentials with an extended range of validity are derived from quantum chromodynamics. Using these potentials the spectra of the quarkonium bound states are calculated and compared with experimental results. This provides a new approach for determining the masses of the charm and bottom quark.

Zusammenfassung

In dieser Arbeit wird die Wechselwirkung zwischen einem schweren Quark und seinem Antiquark untersucht. Durch die Kombination von perturbativen und nicht-perturbativen Methoden werden Wechselwirkungspotentiale mit einem erweiterten Gültigkeitsbereich aus der Quantenchromodynamik abgeleitet. Mit diesen Potentialen werden die Spektren der gebundenen Quarkonium-Zustände berechnet und mit experimentellen Resultaten verglichen. Dadurch ergibt sich ein neuer Zugang zur Bestimmung der Massen des Charm- und Bottom-Quarks.

Contents

1 Introduction

In the last decade large progress has been made in the field of heavy quarkonium physics. Several experiments, primarily BaBar at SLAC, Belle at KEK and CLEO at CESR, contributed to increase the data on quarkonium spectra and decays enormously. A few conventional charmonium and bottomonium states were discovered and more than a dozen quarkonium-like states (e.g., X(3872) and Y(4260)) were found outside the quark model. Effective field theories (EFTs) have been improved and led to a better understanding of quarkonia. Large progress was also made in the field of lattice QCD (quantum chromodynamics), not only due to the constantly increasing computer power.

Since heavy quarkonia are multiscale systems, different sectors of QCD can be probed. In particular, heavy quarkonia are ideal objects to investigate the interplay of perturbative and non-perturbative physics.

In this work, perturbative potentials for charmonium and bottomonium are derived from QCD at different orders in inverse powers of the heavy-quark mass m. These potentials are constructed such that they are reliable from extremely small up to intermediate distances. They are matched to potentials derived within lattice QCD. This matching procedure works well for the leading-order static potential as well as for the $1/m$-potential. The charmonium and bottomonium spectrum is derived at order $1/m$ with a single free parameter from the matched potentials. The value of the single parameter can be obtained by comparing with the experimental spectra. This allows for an accurate extraction of the charm and bottom quark mass.

The non-perturbative part of the charmonium spin-spin potential was obtained recently with high accuracy in a new lattice QCD approach. We extend this lattice potential to short distances by matching it at an intermediate distance scale to a suitable perturbative potential. One-gluon exchange is, in fact, sufficient to derive the corresponding perturbative potential if the running of the QCD coupling $\alpha_s(q)$ is included. The hyperfine splittings in the S-wave charmonium states, derived from the matched spin-spin potential, are then compared with experimental values.

The thesis is organized as follows. In *Chapter 2* basic properties of non-relativistic QCD are introduced and different definitions of the heavy-quark mass are illustrated. The static potential (i.e., the potential between two infinitely heavy quarks) is discussed in *Chapter 3*. An alternative definition of the static perturbative coordinate-space potential via a restricted Fourier transformation

is introduced. This enables the matching with the static potential derived in lattice QCD. *Chapter 4* extends the methods applied for the static potential to the potential at order $1/m$. An analysis of the quark-antiquark potential at order $1/m^2$, where spin-dependency starts to play a role, is done in *Chapter 5*. In *Chapter 6* new lattice QCD results for charmonium, derived from Nambu-Bethe-Salpeter amplitudes through an effective Schrödinger equation, are introduced and extended to short distances by matching with corresponding perturbative potentials. *Chapter 7* deals with quarkonium spectroscopy and the derivation of the charm and bottom quark mass. Spectroscopy is discussed for the static potential, the $1/m$-potential and also for the potentials that are based on the new lattice results. Furthermore, it is shown how to obtain the charm- and bottom-quark mass in our approach and how to translate it to the modified minimal subtraction ($\overline{\text{MS}}$) scheme. The central results of the work are summarized in *Chapter 8*. Finally, the *Appendix* deals with the running of the strong coupling, it shows how to account for flavor thresholds, and it collects results from one-gluon exchange.

2 Theories for heavy quarkonium systems

2.1 Quantum chromodynamics

Quantum chromodynamics (QCD) is the part of the standard model of particle physics that deals with the strong interaction. It is a Yang-Mills theory based on the SU(3) group with six Dirac fields (quarks) of different masses. The charges are usually referred to as color charges and are mediated by exchange particles called gluons. The QCD Lagrangian reads,

$$\mathcal{L}_{\mathrm{QCD}} = \sum_q \overline{\psi}_q (i\gamma^\mu D_\mu - m_q)\psi_q - \frac{1}{4} G^a_{\mu\nu} G^{a\,\mu\nu} \,, \tag{2.1}$$

where $q = u, d, c, s, t, b$, $G^a_{\mu\nu} = \partial_\mu A^a_\nu - \partial_\nu A^a_\mu - g f^{abc} A^b_\mu A^c_\nu$ and $D_\mu = \partial_\mu + i g A^a_\mu T^a$. The generators T^a and the SU(3) structure constants f^{abc} fulfill the relation:

$$[T^a, T^b] = i f^{abc}\, T^c \,. \tag{2.2}$$

The coupling strength of QCD varies under the renormalization group and is characterized by the beta function (see Appendix A.1). At very high energies the interaction between quarks and gluons becomes weak (asymptotic freedom). QCD has at low energies an intrinsic scale Λ_{QCD} which provides the main contribution to the masses of the hadrons. The quarks are usually divided in light quarks $m_u, m_d, m_s \ll \Lambda_{\mathrm{QCD}}$ and heavy quarks $m_c, m_b, m_t \gg \Lambda_{\mathrm{QCD}}$. The physical spectrum consists only of color-singlet states. The u, c and t quarks carry the electric charge $+2/3$, whereas the d, s and b quarks have the electric charge $-1/3$.

2.2 Basic properties of non-relativistic QCD

Heavy quarkonia are systems composed of a heavy quark and its antiquark. The mass m of each quark is much larger than the QCD confinement scale Λ_{QCD}. The system is non-relativistic and is characterized by the heavy-quark velocity $v \ll 1$. For detailed reports about heavy quarkonium physics see Refs. [1, 2].

The study of a non-relativistic heavy quark and its antiquark has a long tradition. After the discovery of the J/ψ meson, Appelquist and Politzer showed [3] that non-relativistic quantum mechanics should be a good approximation to heavy-quark-antiquark systems. But the observed charmonium and bottomonium spectra turned out to be very different compared to a system like positronium. It was found that perturbation theory fails to describe the long-distance part of the heavy-quark potential. Potential models emerged: they incorporated a linear-rising potential and were quite successful. However, they could not be used for quantitative tests of QCD.

A new approach to describe quarkonia was proposed in Refs. [4, 5] where QCD is reformulated in terms of an effective non-renormalizable Lagrangian. The theory is called non-relativistic QCD (NRQCD) and allows to deal with the UV-divergences that appear in the relativistic corrections to the non-relativistic Schrödinger equation. However, the original theory of NRQCD is inconsistent in dimensional regularization and has no consistent power counting in v.

The Lagrangian up to order $1/m^2$ reads:

$$\begin{aligned}\mathcal{L}_{\mathrm{NRQCD}} = \overline{\Psi}\Bigg\{ & i\gamma^0 D_0 + \frac{\vec{D}^2}{2m} + c_F\, g\frac{\vec{\Sigma}\cdot\vec{B}}{2m} + c_D\, g\frac{\gamma^0(\vec{D}\cdot\vec{E} - \vec{E}\cdot\vec{D})}{8m^2} \\ & + ic_S\, g\frac{\gamma^0\,\vec{\Sigma}\cdot(\vec{D}\times\vec{E} - \vec{E}\times\vec{D})}{8m^2}\Bigg\}\Psi \\ & - \frac{1}{4}G^a_{\mu\nu}G^{a\,\mu\nu} + \frac{d_2}{m^2}G^a_{\mu\nu}\vec{D}^2G^{a\,\mu\nu} + \frac{d_3}{m^2}gf^{abc}G^a_{\mu\nu}G^b_{\mu\alpha}G^c_{\nu\alpha} \\ & + \frac{d_{ss}}{m^2}\psi^\dagger\psi\,\chi^\dagger\chi + \frac{d_{sv}}{m^2}(\psi^\dagger\vec{\sigma}\,\psi)\cdot(\chi^\dagger\vec{\sigma}\,\chi) \\ & + \frac{d_{vs}}{m^2}\psi^\dagger T^a\psi\,\chi^\dagger T^a\chi + \frac{d_{vv}}{m^2}(\psi^\dagger T^a\vec{\sigma}\,\psi)\cdot(\chi^\dagger T^a\vec{\sigma}\,\chi)\,, \end{aligned} \tag{2.3}$$

where $\Psi = \psi + \chi$, $\vec{\Sigma} = \left(\begin{smallmatrix}\vec{\sigma} & 0\\ 0 & \vec{\sigma}\end{smallmatrix}\right)$, $D_0 = \partial_0 + igA_0^aT^a$, $\vec{D} = \vec{\nabla} - ig\vec{A}^aT^a$, $E^i = G^{a\,i0}T^a$, ψ is the Pauli-spinor field that annihilates the fermion and χ is the Pauli-spinor field that creates the antifermion. The coefficients c_F, c_D, c_S, d_2, d_3 can be found in Ref. [6] and d_{ss}, d_{sv}, d_{vs}, d_{vv} in Ref. [7].

The modern approach is to use the framework of effective field theories (EFTs). One takes advantage of the existing hierarchy of scales and constructs theories that are simpler than QCD but give equivalent results in the range of interest. The high-energy scales that are not relevant for the non-relativistic heavy quarkonium system can be integrated out during the matching procedure.

The EFT potential NRQCD (pNRQCD) [8, 9] is based on a complete separation of the modes that fluctuate in the various momentum regions. A strict expansion in energy and momentum components that are small in a given region allows for this separation. In pNRQCD, in addition to the hard scale m, also the soft scale mv is integrated out (see next section). The pNRQCD Lagrangian

reads (weak-coupling regime):

$$\begin{aligned}\mathcal{L}_{\rm pNRQCD} = {\rm Tr}\,\Bigg\{ {\rm S}^\dagger \bigg(i\partial_0 - \frac{\vec{p}^{\,2}}{m} - V_s^{(0)} - \frac{V_s^{(1)}}{m} - \frac{V_s^{(2)}}{m^2} + \dots \bigg) {\rm S} \\ + {\rm O}^\dagger \bigg(iD_0 - \frac{\vec{p}^{\,2}}{m} - V_o^{(0)} + \dots \bigg) {\rm O} \Bigg\} \\ + g\, V_A\, {\rm Tr}\left\{ {\rm O}^\dagger\, \vec{r}\cdot\vec{E}\, {\rm S} + {\rm S}^\dagger\, \vec{r}\cdot\vec{E}\, {\rm O} \right\} \\ + g\frac{V_B}{2}\, {\rm Tr}\left\{ {\rm O}^\dagger\, \vec{r}\cdot\vec{E}\, {\rm O} + {\rm O}^\dagger {\rm O}\, \vec{r}\cdot\vec{E} \right\} - \frac{1}{4} G^a_{\mu\nu} G^{a\,\mu\nu}\,, \end{aligned} \tag{2.4}$$

where S and O are the singlet and octet fields, respectively. The functions V are matching coefficients that depend typically on $\vec{r}$ and also on other parameters such as m (via logarithms) or the spin. The focus of this work will be on the singlet potentials $V_s^{(0)}$, $V_s^{(1)}$ and $V_s^{(2)}$.

2.3 Scales and regimes in potential NRQCD

Various scales are involved in heavy quarkonium systems: the hard scale m, the soft scale mv, the ultrasoft scale mv^2 and $\Lambda_{\rm QCD}$. In NRQCD only the hard scale is integrated out and only the condition $m \ll mv, mv^2, \Lambda_{\rm QCD}$ is used. In pNRQCD the soft scale mv is integrated out in addition. This means that only the ultrasoft degrees of freedom (with energies $\sim mv^2$) remain dynamical.

The theory pNRQCD results from a two-step procedure. Starting from QCD, the off-shell degrees of freedom in the hard region are integrated out at the scale $\mu = m$. The resulting theory (NRQCD) is then scaled down to $\mu = mv$ and the scale of the momentum transfer (i.e., the soft scale mv) can be integrated out in such a way that pNRQCD is equivalent to NRQCD up to the required order.

Two situations are possible. So far we have assumed to be in the weak-coupling regime where the soft scale is much larger than $\Lambda_{\rm QCD}$. This means the scales are ordered in the following way: $m \gg mv \gg mv^2 \gtrsim \Lambda_{\rm QCD}$. Perturbative matching of NRQCD and pNRQCD is possible and the matching coefficients V in Eq. (2.4) can be calculated in perturbation theory.

In the second case, the strong-coupling regime, the soft scale is of the order of $\Lambda_{\rm QCD}$ ($m \gg mv \gtrsim \Lambda_{\rm QCD} \gg mv^2$). This implies that the soft scale is non-perturbative and the matching of NRQCD and pNRQCD cannot be performed in perturbation theory. The singlet potential (at leading order, at order $1/m$ and at order $1/m^2$) involves non-perturbative parts given in terms of the static Wilson loop and field-strength insertions in the static Wilson loop. In this regime of pNRQCD, the evaluation of the potentials require non-perturbative methods such as lattice QCD.

2.4 Heavy-quark masses

Like coupling constants, quark masses are no physical observables but parameters of the Lagrangian. This means that, in principle, any well defined quark mass can be used as long as it fulfills certain properties such as being gauge-independent and infrared-finite. In the previous sections, the pole mass definition was understood. The pole mass is indeed gauge-independent and infrared-finite [10] but is usually not suitable for the analysis of experimental data since it generates large perturbative corrections. These artificially large corrections can be interpreted as an ambiguity of the pole-mass definition of the order $\Lambda_{\rm QCD}$ caused by a strong sensitivity to small momenta [11]. The value of the pole mass is shifted by higher-order corrections and is therefore an order-dependent quantity. It was found by Beneke [12] and Hoang *et al.* [13] that the ambiguity of order $\Lambda_{\rm QCD}$ is unphysical but the total static energy,

$$E_{\rm static} = 2m_{\rm pole} + V_s^{(0)}\,, \tag{2.5}$$

is free of this ambiguity.

The problem of the pole-mass definition can be avoided by using a quark mass definition that is less sensitive to low momenta and does not contain the static-quark self-energy in the mass counter term. Such quark masses are called short-distance masses. For example the well known $\overline{\rm MS}$ (modified minimal subtraction) mass falls into this category.

Several quark-mass definitions exist in the literature for certain situations where the quark virtuality is small. Historically the first one was the kinetic mass. It has been proposed in Ref. [14] and is designed for the description of B mesons. It is constructed as the pole mass minus certain matrix elements that are defined within heavy-quark effective theory and describe the difference between the pole mass and the B-meson mass.

The potential-subtracted (PS) mass $m_{\rm PS}$ has been proposed by Beneke in Ref. [12] and is defined as:

$$m_{\rm PS}(\mu_{\rm PS}) = m_{\rm pole} + \frac{1}{2}\int\limits_{|\vec{q}|<\mu_{\rm PS}} \frac{d^3\vec{q}}{(2\pi)^3}\,\tilde{V}_s^{(0)}(\vec{q})\,, \tag{2.6}$$

where $\tilde{V}_s^{(0)}$ is the static color-singlet potential in momentum space. The PS mass depends on the scale $\mu_{\rm PS}$ that serves as a cutoff for the self-energy integration. We will use this scheme in the subsequent chapters.

Another quark mass, the 1S mass, has been proposed in Ref. [15]. It is defined as half of the perturbative series for the mass of the $1^3{\rm S}_1$ quarkonium state. It is scale independent but has in general small perturbative uncertainties.

Finally, the renormalon-subtracted (RS) mass has been proposed in Ref. [16]. It depends on the scale $\mu_{\rm RS}$ and is defined as the perturbative series where all non-analytic pole terms from the Borel transform of the pole-$\overline{\rm MS}$-mass relation

at $u = 1/2$ have been subtracted (see Section 3.2.3). The terms in the relation between the pole mass and the RS mass are formally known to all orders, but the numerical value of the coefficients of the series are only approximately known due to subleading contributions.

For a detailed overview of the different schemes we refer to Ref. [11].

3 The static potential

3.1 Studies within lattice QCD

Lattice QCD works in a discrete Euclidean space-time to evaluate the QCD path integral numerically. Using Monte Carlo integration, vacuum expectation values of numerous operators are studied. Systematic errors such as effects due to the finite lattice spacing are well controlled.

The potential between two static color sources is one of the most precisely determined quantities in lattice QCD. It is related to the static Wilson loop and has been studied for many years in the so called quenched approximation. This approximation neglects vacuum polarization effects that arise from dynamical fermions. A linear confining potential at distances much larger than one femtometer is observed, since string breaking is forbidden in such a configuration (see, e.g., [17]). The quenched approximation can be dropped nowadays due to rapidly increasing computer power.[1] A comparison of a quenched static potential with a potential where two flavors of dynamical Wilson fermions are included is shown in Fig. 3.1. One finds that the un-quenched data points lie systematically below their quenched counterparts at short distances, even though it is a small effect.

In this chapter, we will use the lattice QCD results of Ref. [18] to continue perturbative results of static charmonium and bottomonium potentials (valid at short and intermediate distances) to distances up to approximately one femtometer. An extrapolation to the physical pion mass (i.e., to realistic light-quark masses) has already been performed in Ref. [18]. The authors find the values $e = 0.368^{+0.020}_{-0.026}$ and $\sqrt{\sigma} = (0.447^{+0.022}_{-0.024})$ GeV and use a parametrization of the form:

$$V^{(0),\,\mathrm{lat}}(r) = -\frac{e}{r} + \sigma\, r + \mathrm{const}\,. \tag{3.1}$$

The error of the string tension σ stems mainly from the uncertainty of the Sommer scale, $r_0 = 0.50 \pm 0.03$ fm.

[1] The quenched approximation is still used for specific problems. For example for studies of the mass dependent potentials (see Chapters 4 and 5).

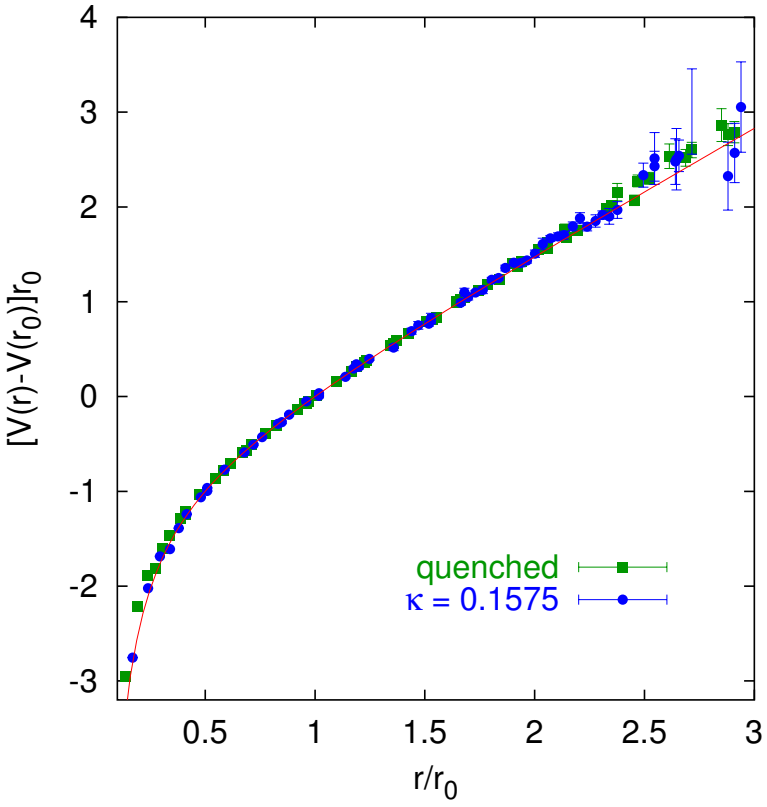

Figure 3.1: The static potential from lattice QCD ($r_0 \approx 0.5$ fm). Comparison between quenched results and un-quenched results (with a mass parameter value $\kappa = 0.1575$). Plot adapted from Ref. [18].

3.2 Definition of the perturbative potential

3.2.1 Momentum-space potential to order N^{3}LO

The perturbative static potential (i.e., the color-singlet potential between two infinitely heavy quarks) has been derived over the years from QCD with steadily increasing precision. It can be written in momentum space in the compact form:

$$\tilde{V}^{(0)}(|\vec{q}|) = -\frac{4\pi C_F \alpha_s(|\vec{q}|)}{\vec{q}^{\,2}} \left\{ 1 + \frac{\alpha_s(|\vec{q}|)}{4\pi}\, a_1 + \left(\frac{\alpha_s(|\vec{q}|)}{4\pi}\right)^2 a_2 + \left(\frac{\alpha_s(|\vec{q}|)}{4\pi}\right)^3 \left(a_3 + 8\pi^2 C_A^3 \ln \frac{\mu_{\rm IR}^2}{\vec{q}^{\,2}} \right) + \mathcal{O}\left(\alpha_s^4\right) \right\}, \quad (3.2)$$

where $\vec{q}$ is the three-momentum transfer. The coefficients a_1 and a_2 have been known in analytic form for many years in the $\overline{\rm MS}$ scheme [19, 20, 21],

$$a_1 = \frac{31}{9}C_A - \frac{20}{9}T_F n_f, \tag{3.3}$$

$$a_2 = \left(\frac{4343}{162} + 4\pi^2 - \frac{\pi^4}{4} + \frac{22}{3}\zeta(3)\right) C_A^2 - \left(\frac{1798}{81} + \frac{56}{3}\zeta(3)\right) C_A T_F n_f - \left(\frac{55}{3} - 16\zeta(3)\right) C_F T_F n_f + \left(\frac{20}{9}T_F n_f\right)^2, \tag{3.4}$$

where $C_F = 4/3$, $C_A = 3$, $T_F = 1/2$ for SU(3) and n_f is the number of light quark flavors. At three-loop order, infrared-singular contributions proportional to $\ln(\mu_{\rm IR}^2/\vec{q}^{\,2})$ start to play a role (see, e.g., [22]). The accompanying constant

$$a_3 = 64\,(209.884(1) - 51.4048 n_f + 2.9061 n_f^2 - 0.0214 n_f^3) \tag{3.5}$$

has been calculated independently in [23] and [24].

3.2.2 Analytic transformation to coordinate space

In order to transform the potential to coordinate space, $\alpha_s(|\vec{q}\,|)$ in Eq. (3.2) is usually expressed as a powers series expansion in $\alpha_s(\mu)$ at some fixed scale μ:

$$\begin{aligned}\alpha_s(q) = \alpha_s(\mu)\Bigg[1 &- \frac{\alpha_s(\mu)}{4\pi}\beta_0\,\ell + \left(\frac{\alpha_s(\mu)}{4\pi}\right)^2 (\beta_0^2\,\ell - \beta_1)\,\ell \\ &+ \left(\frac{\alpha_s(\mu)}{4\pi}\right)^3 \left(-\beta_0^3\,\ell^2 + \frac{5}{2}\beta_0\beta_1\,\ell - \beta_2\right)\ell \\ &+ \left(\frac{\alpha_s(\mu)}{4\pi}\right)^4 \left(\beta_0^4\,\ell^3 - \frac{13}{3}\beta_0^2\beta_1\,\ell^2 + 3\Big(\beta_0\beta_2 + \frac{\beta_1^2}{2}\Big)\ell - \beta_3\right)\ell \\ &+ \mathcal{O}\left(\alpha_s^5\right)\Bigg],\end{aligned} \tag{3.6}$$

with $\ell = \ln(q^2/\mu^2)$. This formula is derived in Section A.1 in the Appendix. The values of the coefficients of the β-function β_n are also listed in Section A.1.

A Fourier transform of the momentum-space potential, where $\alpha_s(|\vec{q}\,|)$ has been expanded according to Eq. (3.6), leads to the standard, μ-dependent defi-

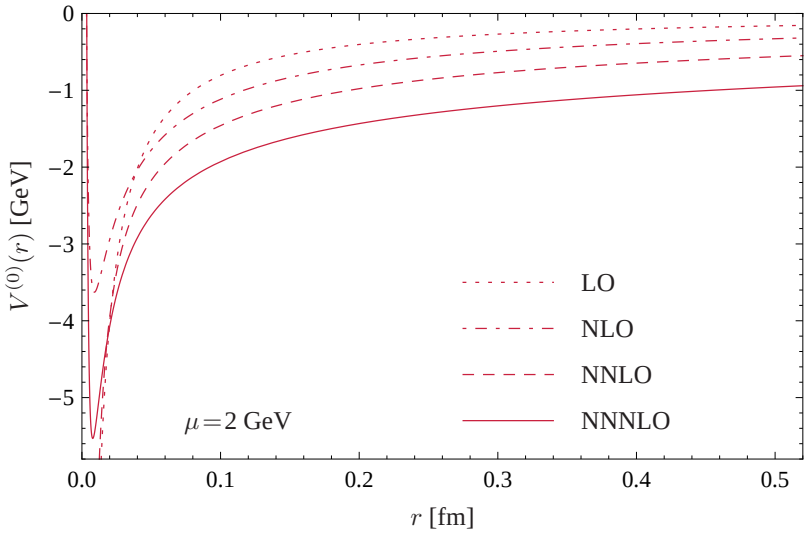

Figure 3.2: Static r-space potential according to Eq. (3.7) using $\mu = 2$ GeV. The choice $\mu_{\rm IR}^2 = \vec{q}^{\,2}$ has been adopted at NNNLO.

nition of the coordinate-space static potential,

$$V^{(0)}(r) = -\frac{4\,\alpha_s(\mu)}{3\,r}\left\{1 + \frac{\alpha_s(\mu)}{4\pi}\left[a_1 + 2\beta_0\, g_\mu(r)\right]\right.$$
$$+ \left(\frac{\alpha_s(\mu)}{4\pi}\right)^2\left[a_2 + \beta_0^2\big(4g_\mu^2(r) + \pi^2/3\big) + 2g_\mu(r)(2a_1\beta_0 + \beta_1)\right]$$
$$+ \left(\frac{\alpha_s(\mu)}{4\pi}\right)^3\left[a_3 + 16\pi^2 C_A^3\big(\ln(\mu_{\rm IR} r) + \gamma_{\rm E}\big) + \beta_0^3\big(8g_\mu^3(r) + 2\pi^2 g_\mu(r) + 16\zeta(3)\big)\right.$$
$$\left.\left. + \beta_0\big(12g_\mu^2(r) + \pi^2\big)\big(a_1\beta_0 + 5/6\,\beta_1\big) + 2g_\mu(r)\big(3a_2\beta_0 + 2a_1\beta_1 + \beta_2\big)\right] + \mathcal{O}(\alpha_s^4)\right\}, \tag{3.7}$$

where $g_\mu(r) = \ln(\mu r) + \gamma_{\rm E}$. The derivation of this r-space potential uses, in principle, information about $\alpha_s(|\vec{q}\,|)$ over the full range in q space. However, the expansion (3.6) in powers of $\ln q^2$ is a good approximation only in a small neighborhood of the scale μ, as illustrated in Fig. A.1 in the Appendix. Clearly, the behavior of $\alpha_s(q)$ for $q > 10$ GeV and $q < 1$ GeV is out of control for such an expansion.

Fixing μ for instance at 2 GeV, the resulting coordinate-space potential (3.7) behaves pathologically at $r \to 0$, as shown in Fig. 3.2. This behavior can be traced to the order-by-order sign changes of Eq. (3.6) for $q \to \infty$. Figure 3.3 shows the potential (3.7) resulting from the frequently used *ad hoc* identification $\mu = 1/r$ which evidently works only at extremely short distances, $r < 0.02$ fm.

The perturbative potential as defined in Eq. (3.7) does not indicate convergence and is obviously not suitable as a foundation for a reliable potential that is valid over a large distance space.

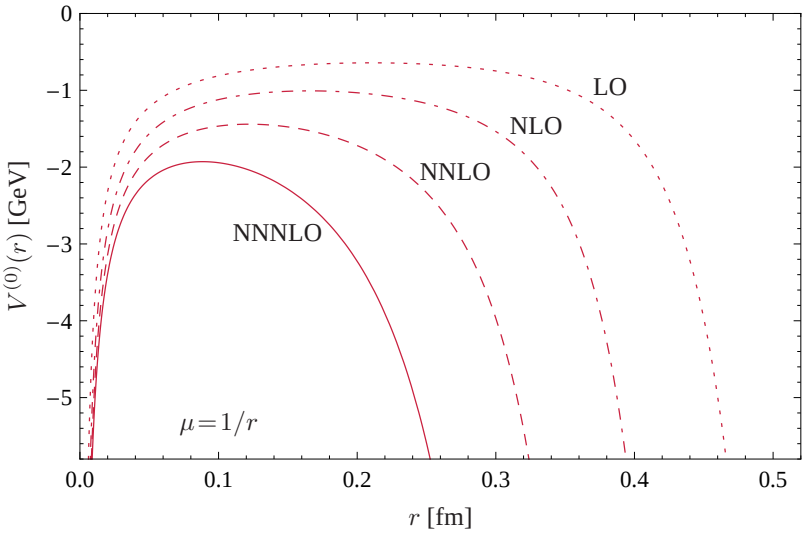

Figure 3.3: Static r-space potential according to Eq. (3.7). Progressive orders are shown when μ is identified with $1/r$. The choice $\mu_{\rm IR}^2 = \vec{q}^{\,2}$ has been adopted at NNNLO.

3.2.3 Renormalon-subtraction scheme

It was realized in Ref. [25] that the static potential suffers from renormalons, which are singularities in the Borel plane. The Borel transform is defined as,

$$B[R](u) = \sum_{n=0}^{\infty} r_n \, \frac{u^n}{n!} \,, \tag{3.8}$$

for a divergent series expansion $R \sim \sum_{n=0}^{\infty} r_n \alpha^n$ of R. It is found that the momentum-space potential $\tilde{V}^{(0)}(|\vec{q}\,|)$ is free of renormalon contributions of order $\Lambda_{\rm QCD}/|\vec{q}\,|$. The leading effect due to renormalons is instead of order $\Lambda_{\rm QCD}^2/\vec{q}^{\,2}$:

$$\tilde{V}^{(0)}(|\vec{q}\,|) = -\frac{4\pi\, C_F\, \alpha_s}{\vec{q}^{\,2}} \left(1 + \ldots + \text{const} \times \frac{\Lambda_{\rm QCD}^2}{\vec{q}^{\,2}} + \ldots \right). \tag{3.9}$$

However, the coordinate-space potential $V^{(0)}(r)$ has a pole at $u = 1/2$ in the Borel plane that amounts to a r-independent overall constant of order $\Lambda_{\rm QCD}$ in $V^{(0)}(r)$:

$$V^{(0)}(r) = -\frac{C_F\, \alpha_s}{r} \left(1 + \ldots + \text{const} \times \Lambda_{\rm QCD}\, r + \ldots \right). \tag{3.10}$$

It is shown in the Refs. [12, 13] that the sum of $V^{(0)}(r)$ and twice the heavy-quark pole mass is free of leading renormalon effects. See Ref. [26] for an comprehensive review of renormalons.

The potential of Eq. (3.7) can be improved by using the renormalon-subtraction (RS) scheme [16]. A detailed study and a comparison of the static perturbative potential with lattice QCD in the RS scheme has been done in Ref. [27].

3.2.4 Potential-subtracted scheme

Here we pursue a different strategy for constructing the static potential in coordinate space. It is based on the potential-subtracted (PS) scheme proposed by M. Beneke [12] and has been published in Ref. [28]. The r-space potential is defined through a restricted Fourier transform as

$$V^{(0)}(r,\mu_f) = \int\limits_{|\vec{q}|>\mu_f} \frac{d^3q}{(2\pi)^3}\; e^{i\vec{q}\cdot\vec{r}}\,\tilde{V}^{(0)}(|\vec{q}|)\,, \tag{3.11}$$

where $\tilde{V}^{(0)}(|\vec{q}|)$ is given in Eq. (3.2), but now $\alpha_s(|\vec{q}|)$ for $|\vec{q}|>\mu_f$ is used without resorting to a power series expansion. The momentum-space cutoff μ_f is introduced in order to delineate the uncontrolled low-q region from the high-q range where perturbation theory is considered to be reliable. The potential (3.11) differs from the "true" static potential,

$$V^{(0)}(r) = v^{(0)}(\mu_f) + V^{(0)}(r,\mu_f)\,, \tag{3.12}$$

approximately by a constant,

$$v^{(0)}(\mu_f) = \int\limits_{|\vec{q}|\le\mu_f} \frac{d^3q}{(2\pi)^3}\; e^{i\vec{q}\cdot\vec{r}}\,\tilde{V}^{(0)}(|\vec{q}|) = \frac{1}{2\pi^2}\int\limits_0^{\mu_f} dq\,q^2\,\tilde{V}^{(0)}(q) + \mathcal{O}(\mu_f^2\,r^2)\,, \tag{3.13}$$

which encodes non-perturbative low-q behavior that can be absorbed in the definition of the potential-subtracted (PS) quark mass (see Section 7.1). The correction of order $\mu_f^2\,r^2$ is negligibly small in the range of interest ($r<0.2$ fm).

The potential $V^{(0)}(r,\mu_f)$ is evaluated numerically using the four-loop renormalization group running of the strong coupling α_s, see Section A.1 of the Appendix. For distances $r<0.2$ fm, the resulting potential depends only weakly on μ_f as shown in Fig. 3.4. At the position $r=0.14$ fm the spread of $(V^{(0)}-\text{const})$ when varying μ_f between 0.7 GeV and 1.5 GeV is 0.05 GeV. The convergence behavior of the potential is displayed in Fig. 3.5. Different orders have been matched at $r=0.01$ fm and are then evolved to larger distances. Evidently, the convergence behavior of the potential $V^{(0)}(r,\mu_f)$ is satisfactory.

For bottomonium ($n_f=4$ massless flavors), the input value for the renormalization group running of the strong coupling constant is chosen as $\alpha_s(4.2\text{ GeV}) = 0.226\pm0.003$. In the case of charmonium ($n_f=3$) we use $\alpha_s(1.25\text{ GeV}) = 0.406\pm0.010$ as input in the potential. These values are obtained from $\alpha_s(m_Z = 91.1876\text{ GeV}) = 0.1184\pm0.0007$ [29] (for a theory with $n_f=5$ active quark flavors) and run down to 4.2 GeV and 1.25 GeV, taking into account flavor thresholds (see Section A.2 of the Appendix for details).

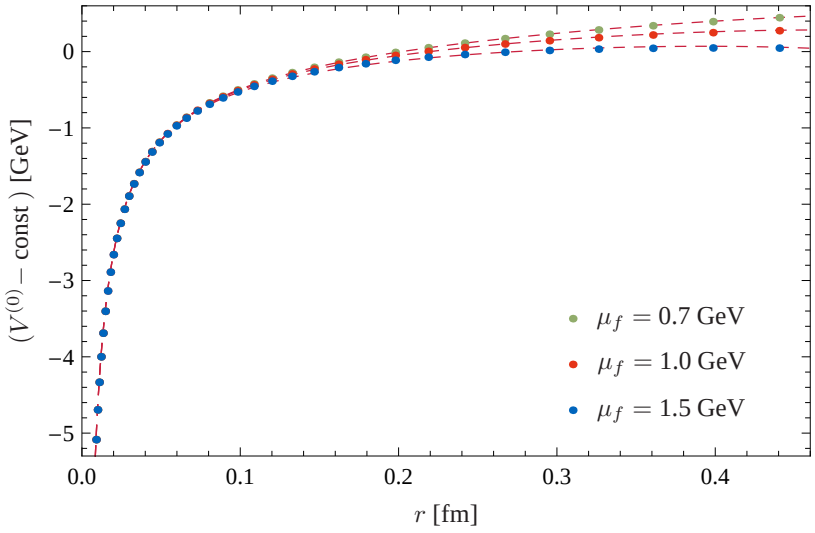

Figure 3.4: Static QCD potential (with $n_f = 3$) from the restricted numerical Fourier transform (3.11). Shown is the NNLO potential for different values of μ_f. The curves have been shifted by a constant to match at small r values.

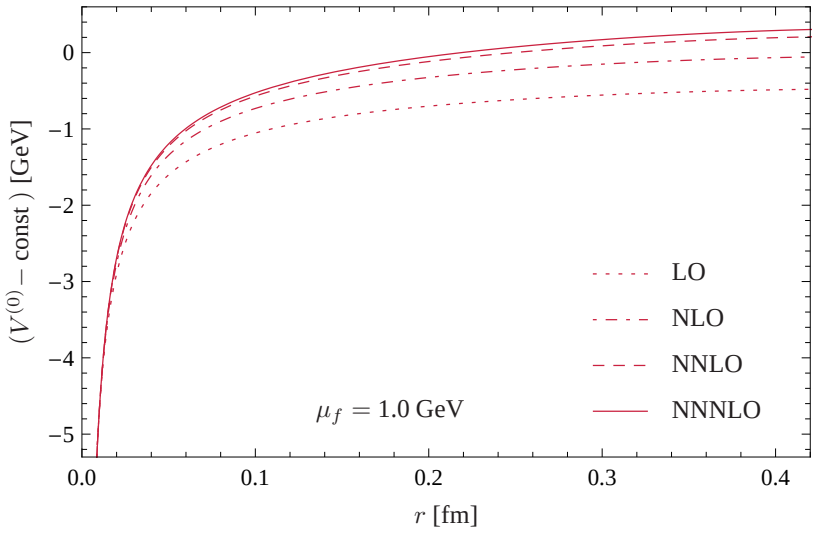

Figure 3.5: Static QCD potential (with $n_f = 3$ and $\mu_f = 1.0$ GeV) from the restricted numerical Fourier transform (3.11). Different orders of have been matched at 0.01 fm. The choice $\mu_{\text{IR}}^2 = \vec{q}^{\,2}$ has been adopted at NNNLO.

3.3 Matching of potentials from perturbative and lattice QCD

The perturbative potential (3.11), valid at small and intermediate distances, can be matched to a potential derived from lattice QCD. We use the lattice

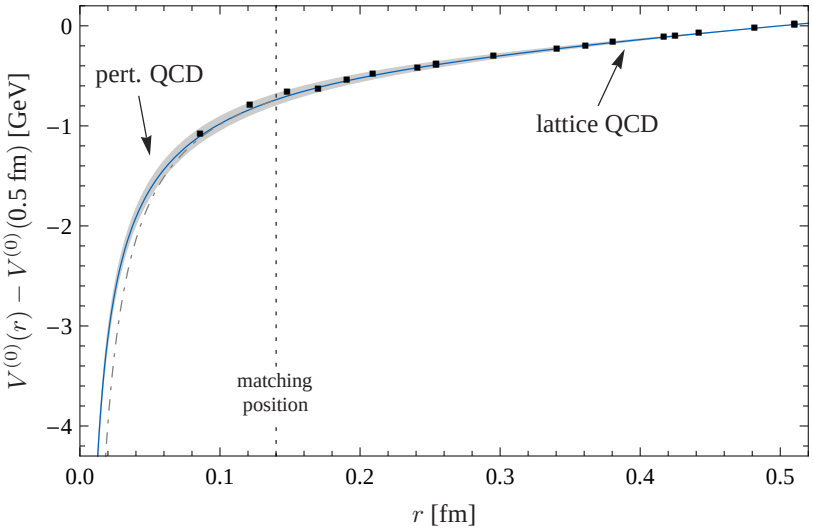

Figure 3.6: Static QCD potential for $n_f = 3$, based on Eqs. (3.11) and (3.2), matched at intermediate distances to a potential from lattice QCD [18]. Dashed-dotted curve: simplest extrapolation using Coulomb-plus-linear r dependence.

results of Ref. [18], as quoted in Section 3.1. The resulting matched static potential is shown in Fig. 3.6. The matching point (dashed line) is chosen at $r = 0.14$ fm. At this position, both the perturbative and the lattice potential are expected to be reliable. The resulting shape of the potential changes only marginally under reasonably constrained variations of the matching position. Requiring that the first derivative of the potential is continuous at the matching point, we find for the cutoff in Eq. (3.11): $\mu_f = 0.908$ GeV (bottomonium case) and $\mu_f = 0.930$ GeV (charmonium case). The grey band reflects uncertainties in the Sommer scale $r_0 = 0.50 \pm 0.03$ fm (lattice part) and uncertainties in $\alpha_s(|\vec{q}|)$ (perturbative part) as given in the previous paragraph. This leads to a cutoff window: $\mu_f = 0.9^{+0.3}_{-0.2}$ GeV (for both bottomonium and charmonium). The dashed-dotted line in Fig. 3.6 results from a simple Coulomb-plus-linear extrapolation from the lattice QCD data to short distances. Evidently, our more sophisticated perturbative QCD extrapolation based on Eqs. (3.11) and (3.2) differs from that simple form.

For zero flavors one can check the reliability of our construction against accurate (quenched) lattice results [30] (see Fig. 3.7). Since α_s cannot be extracted from experiment for $n_f = 0$, we fit to the lattice points below 0.12 fm. With a low momentum cutoff μ_f in the range 0.7–1.5 GeV, we find $\alpha_s(1.25\ \mathrm{GeV}) = 0.29 \pm 0.01$ for the flavorless strong coupling at the scale of the c-quark mass. The lattice scale $r_0 = 0.5$ fm has been used here. A precision study of the zero-flavor case in a different approach can be found in Ref. [31].

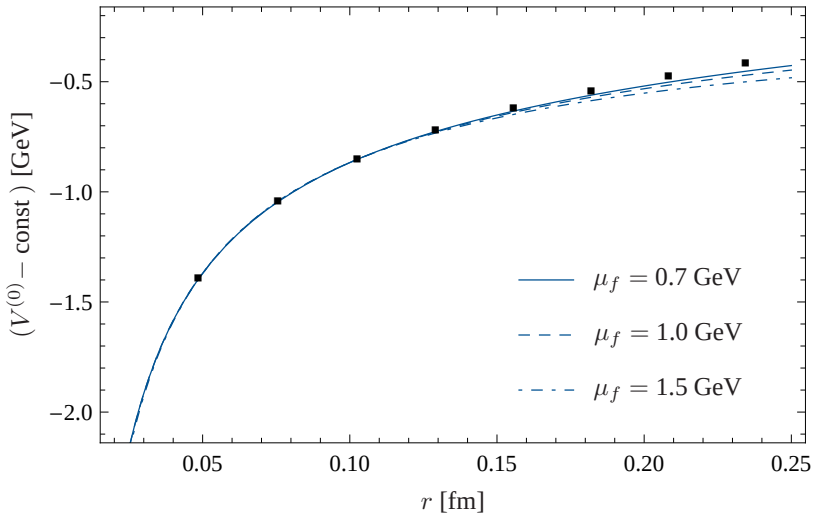

Figure 3.7: The static potential for $n_f = 0$ flavors compared to lattice points [30]. The lattice scale r_0 has been set to 0.5 fm.

3.4 Schrödinger equation and wave functions

Wave functions and quarkonium spectra are defined in the static case by the Schrödinger equation,

$$\left[-\frac{1}{m}\vec{\nabla}^2 + V^{(0)}(r, \mu_f) + v^{(0)}(\mu_f) - E \right] \psi(\vec{r}) = 0\,. \tag{3.14}$$

$V^{(0)}(r, \mu_f)$ is the matched potential either with $n_f = 3$ and $\mu_f = 0.930$ GeV for the charmonium case, or with $n_f = 4$ and $\mu_f = 0.908$ GeV for the bottomonium case. At this point, the parameter $v^{(0)}(\mu_f)$ is in both cases an unknown additive constant.

Equation (3.14) can be solved numerically in order to obtain wave functions and corresponding eigenvalues. The lowest wave functions for $l = 0$ and $l = 1$ are shown in Figs. 3.8 and 3.9. The energy eigenvalues depend on the unknown constant $v^{(0)}(\mu_f)$. The value of $v^{(0)}(\mu_f)$ will be determined by comparing the model predicted charmonium and bottomonium spectra with the empirical ones and can then be used to derive the charm and bottom quark masses (see Chapter 7).

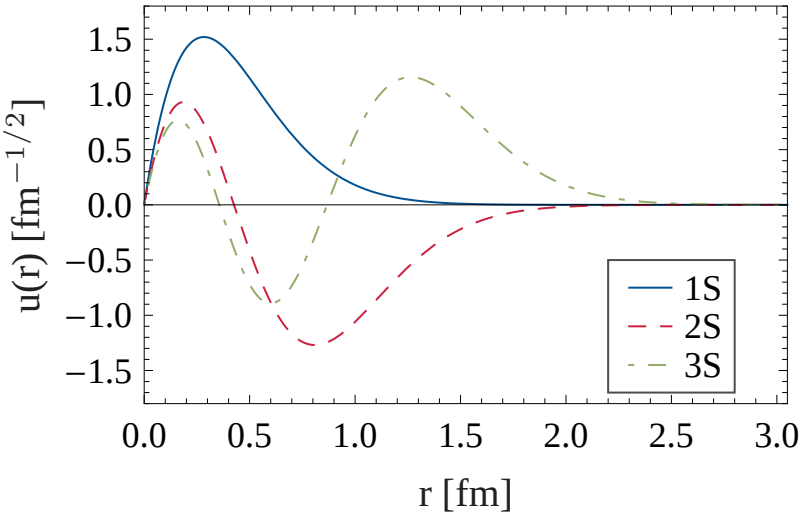

Figure 3.8: Charmonium wave functions ($u(r) = r\psi(r)$). The three lowest S-wave states are shown.

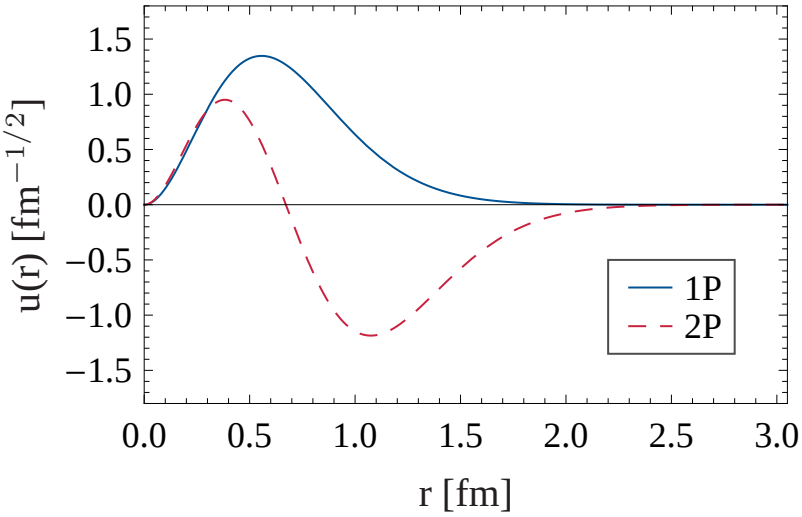

Figure 3.9: Charmonium wave functions ($u(r) = r\psi(r)$). The lowest P-wave states are shown.

4 Quark-antiquark potential at order $1/m$

4.1 Definition within pNRQCD

In the framework of potential non-relativistic QCD (pNRQCD), the static potential emerges at leading order, followed by relativistic corrections in powers of the inverse heavy-quark mass. The $Q\overline{Q}$ potential up to order $1/m$ is usually written as

$$V = V^{(0)}(r) + \left(\frac{1}{m_1} + \frac{1}{m_2}\right) V^{(1)}(r)\,, \tag{4.1}$$

where $V^{(1)}(r)$ is the first quark-mass dependent correction of the static potential $V^{(0)}(r)$. In contrast to the leading order potential, that is known for a long time and corresponds to the static Wilson loop, the complete non-perturbative expression for the $1/m$ term has been derived much later [32]. It is expressed in terms of chromoelectric field insertions in a Wilson loop:

$$V^{(1)} = \lim_{T\to\infty}\Bigg(-\frac{g^2}{4T}\int_{-T/2}^{T/2} dt \int_{-T/2}^{T/2} dt'\,|t-t'| \\ \times\Big[\langle\!\langle \vec{E}(t)\cdot\vec{E}(t')\rangle\!\rangle_\Box - \langle\!\langle \vec{E}(t)\rangle\!\rangle_\Box \cdot \langle\!\langle \vec{E}(t')\rangle\!\rangle_\Box\Big]\Bigg)\,. \tag{4.2}$$

The double angular bracket $\langle\!\langle \ldots \rangle\!\rangle_\Box \equiv \langle \ldots W_\Box\rangle / \langle W_\Box\rangle$ stands for the normalized average over the gauge fields of the rectangular static Wilson loop

$$W_\Box \equiv \mathrm{P}\exp\Big\{ -ig \oint_{r\times T} dz^\mu A_\mu(z)\Big\}\,. \tag{4.3}$$

It is stressed in Ref. [32] that $V^{(1)}$ is not unique and can be reshuffled under certain circumstances via a unitary transformation in $1/m^2$ and higher terms. In the following, the convention introduced above is used.

An evaluation of Eq. (4.2) at leading non-vanishing order in α_s gives [32]:

$$\tilde{V}^{(1)}(|\vec{q}\,|) = -\frac{C_F\, C_A\, \pi^2\, \alpha_s^2(|\vec{q}\,|)}{2\,|\vec{q}\,|}\,, \tag{4.4}$$

with $C_F = 4/3$ and $C_A = 3$. This is in agreement with the result of Refs. [33, 34] performed in perturbation theory.

4.2 Results from lattice QCD

Lattice gauge theory is a commonly used tool to simulate observables in low-energy QCD. It can also be used to investigate the behavior of chromoelectric and chromomagnetic field operators.

The $1/m$ potential has been studied on the lattice for the first time in Ref. [35]. The analysis is based on the non-perturbative expression given in Eq. (4.2). Statistical and systematic errors are reduced by employing the multi-level algorithm (see Refs. [36, 37]) for measuring the field strength correlators on the Polyakov loop correlation function (PLCF). A modification of the method, used to determine the spin-dependent potentials [38, 39], is applied to extract the order $1/m$ potential. The first result [35] has been updated in Ref. [40] and is shown in Fig. 4.1.

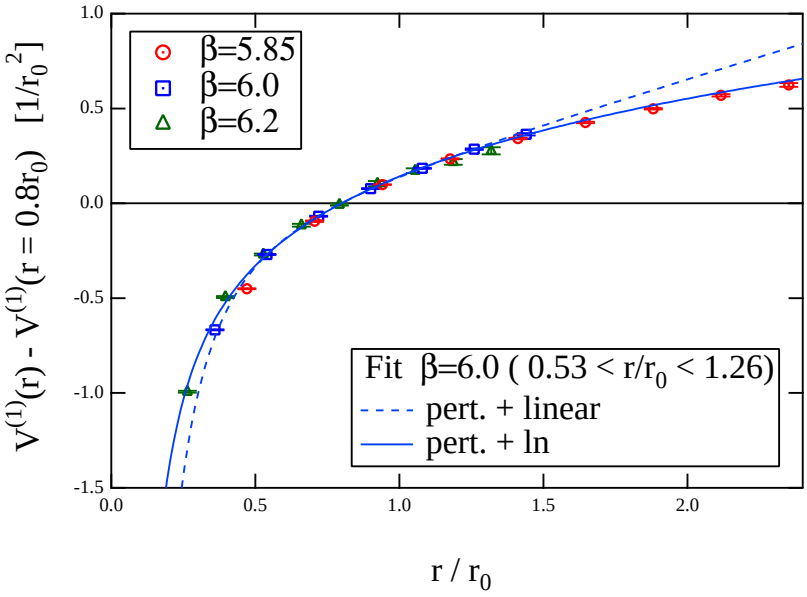

Figure 4.1: Lattice simulation for the QCD potential at order $1/m$ in units of $r_0 \approx 0.5$ fm. Plot is taken from Ref. [40].

Two different functional forms are used to fit the lattice points: both forms involve a $1/r^2$ term to reflect the short-distance perturbative part, but differ in the parametrization of the long-distance part of the $1/m$ potential. To reflect the lattice results at this region, either a linear term or a logarithmic term is added to the $1/r^2$ term. One observes that the logarithmic fit form extrapolates the lattice points better than a linear shape. A logarithmic shape is expected at long distances at order $1/m$ from effective string theory [41]. We use the following fit of lattice results:

$$V_{\rm fit}^{(1)}(r) = -\frac{c'}{r^2} + d' \ln\left(\frac{r}{r'}\right) + \text{const}\,, \tag{4.5}$$

with $c' = 2.7 \cdot 10^{-3}$ GeV^2 fm^2, $d' = 0.075$ GeV^2 and an arbitrary length scale r' that can be absorbed in the overall constant.

4.3 Construction and matching of the potential

The perturbative momentum-space potential $\tilde{V}^{(1)}(|\vec{q}\,|)$, quoted in Eq. (4.4), can be transformed to r-space in a similar way as in the static case. A low momentum cutoff μ_f' is introduced that may differ from μ_f (the cutoff in the static case):

$$V^{(1)}(r, \mu_f') = \int\limits_{|\vec{q}|>\mu_f'} \frac{d^3q}{(2\pi)^3}\; e^{i\vec{q}\cdot\vec{r}}\, \tilde{V}^{(1)}(|\vec{q}\,|)\,. \tag{4.6}$$

Evidently, the dependence of $V^{(1)}$ on the cutoff scale μ_f' is again very weak for distances $r < 0.2$ fm as shown in Fig. 4.2. The variation of $(V^{(1)} - \text{const})$ when varying μ_f' between 0.7 GeV and 1.5 GeV is within 0.02 GeV^2 at the matching radius, $r = 0.14$ fm.

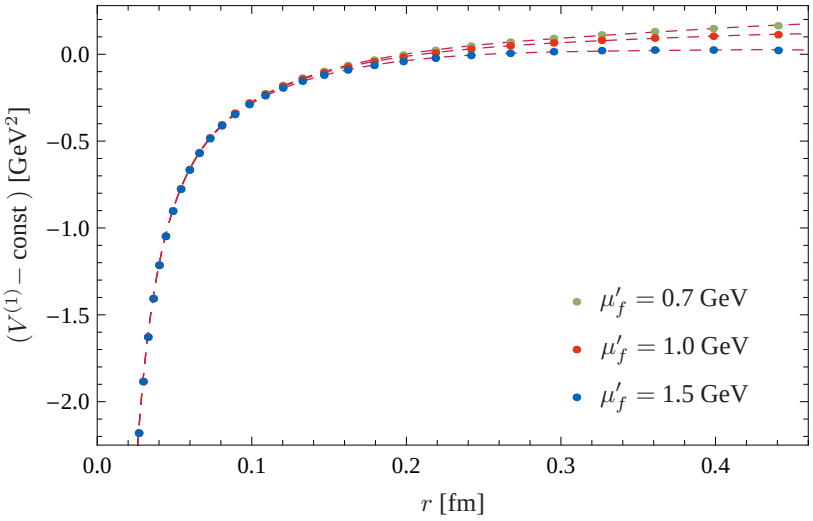

Figure 4.2: The order $1/m$ potential $V^{(1)}(r, \mu_f')$ with $n_f = 3$ from the restricted numerical Fourier transform (4.6), for different cutoffs μ_f'. The curves have been shifted by a constant to match at small r values.

This short distance potential is matched at intermediate distance scales to the $1/m$ potential derived within lattice QCD (see previous section). The lattice calculation of $V^{(1)}$ is quenched and subject to renormalization issues. A 15% uncertainty is therefore assumed in the lattice potential, in addition to the uncertainties in the Sommer scale r_0. At short distances a deviation of the perturbative potential $V^{(1)}(r, \mu_f')$ from $V_{\rm fit}^{(1)}$ of Eq. (4.5) (dashed-dotted line in Fig. 4.3) is apparent. For the cutoff in Eq. (4.6) with error estimate we find:

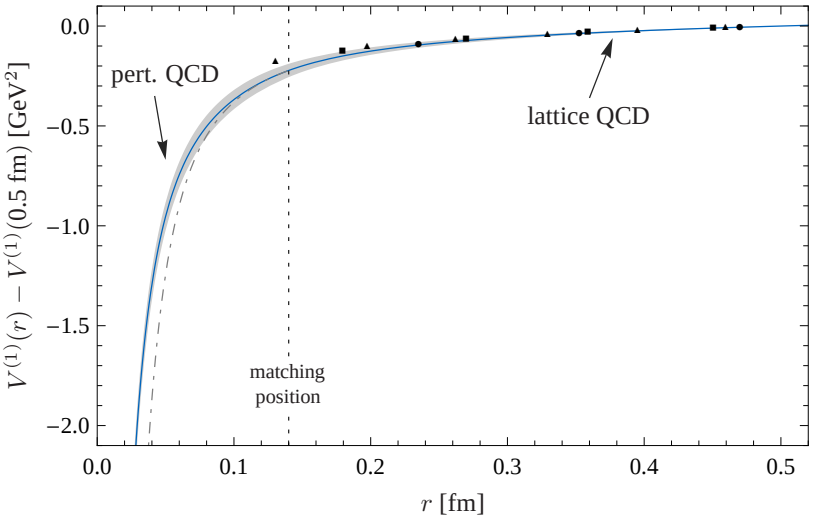

Figure 4.3: The order $1/m$ potential $V^{(1)}(r, \mu_f')$ with $n_f = 3$, based on Eq. (4.6), matched at intermediate distances to a potential from lattice QCD [40]. The fit and the matching has been performed using the lattice QCD points with $\beta = 5.85$ (circles). Legends are analogous to Fig. 3.6. Dashed-dotted curve: simple extrapolation using Eq. (4.5).

$\mu_f' = 1.9^{+0.4}_{-0.6}$ GeV (bottomonium case) and $\mu_f' = 1.6^{+0.5}_{-0.8}$ GeV (charmonium case).

5 Quark-antiquark potential at order $1/m^2$

5.1 Complete non-perturbative expression

The color-singlet potential at order $1/m^2$ between a heavy quark and its antiquark is often written as:

$$V^{(2)} = \frac{V^{(2,0)}}{m_1^2} + \frac{V^{(0,2)}}{m_2^2} + \frac{V^{(1,1)}}{m_1 m_2}\,, \tag{5.1}$$

where m_1 and m_2 denote the masses of the two particles. It is convenient to split $V^{(2,0)}$ and $V^{(0,2)}$ in a spin-dependent and a spin-independent part:

$$V^{(2,0)} = V_{\rm SD}^{(2,0)} + V_{\rm SI}^{(2,0)}\,, \qquad V^{(0,2)} = V_{\rm SD}^{(0,2)} + V_{\rm SI}^{(0,2)}\,. \tag{5.2}$$

The spin-dependent terms can be written as:

$$V_{\rm SD}^{(2,0)} = V_{LS}^{(2,0)}(r)\,\vec{L}_1\cdot\vec{S}_1\,, \tag{5.3}$$

and

$$V_{\rm SD}^{(0,2)} = -V_{LS}^{(0,2)}(r)\,\vec{L}_2\cdot\vec{S}_2\,. \tag{5.4}$$

Note that $\vec{L}_1$ and $\vec{L}_2$ are not the orbital angular momenta of the two heavy quarks. They are defined as:

$$\vec{L}_1 \equiv \vec{r}\times\vec{p}_1\,, \qquad \vec{L}_2 \equiv \vec{r}\times\vec{p}_2\,, \tag{5.5}$$

with $\vec{r} = \vec{r}_1 - \vec{r}_2$ the relative coordinate vector of the quark and the antiquark. The spin-independent parts of $V^{(2,0)}$ and $V^{(0,2)}$ can be decomposed as:

$$V_{\rm SI}^{(2,0)} = \frac{1}{2}\left\{\vec{p}_1^{\,2}, V_{p^2}^{(2,0)}(r)\right\} + \frac{V_{L^2}^{(2,0)}(r)}{r^2}\,\vec{L}_1^2 + V_r^{(2,0)}(r)\,, \tag{5.6}$$

and

$$V_{\rm SI}^{(0,2)} = \frac{1}{2}\left\{\vec{p}_2^{\,2}, V_{p^2}^{(0,2)}(r)\right\} + \frac{V_{L^2}^{(0,2)}(r)}{r^2}\,\vec{L}_2^2 + V_r^{(0,2)}(r)\,. \tag{5.7}$$

The $V^{(1,1)}$ potential is separated in a similar way in a spin-dependent and a spin-independent part:

$$V^{(1,1)} = V_{\rm SD}^{(1,1)} + V_{\rm SI}^{(1,1)}\,. \tag{5.8}$$

The two terms defined as:

$$V_{\rm SD}^{(1,1)} = V_{L_1S_2}^{(1,1)}(r)\,\vec{L}_1\cdot\vec{S}_2 - V_{L_2S_1}^{(1,1)}(r)\,\vec{L}_2\cdot\vec{S}_1 + V_{S^2}^{(1,1)}(r)\,\vec{S}_1\cdot\vec{S}_2 + V_{\vec{S}_{12}}^{(1,1)}(r)\,\vec{S}_{12}\,, \quad (5.9)$$

where $\vec{S}_{12} \equiv 12(\hat{r}\cdot\vec{S}_1)(\hat{r}\cdot\vec{S}_2) - 4(\vec{S}_1\cdot\vec{S}_2)$, and

$$V_{\rm SI}^{(1,1)} = -\frac{1}{2}\left\{\vec{p}_1\cdot\vec{p}_2, V_{p^2}^{(1,1)}(r)\right\} - \frac{V_{L^2}^{(1,1)}(r)}{2r^2}\,(\vec{L}_1\cdot\vec{L}_2 + \vec{L}_2\cdot\vec{L}_1) + V_r^{(1,1)}(r)\,. \quad (5.10)$$

Non-perturbative expressions for all potentials introduced above have been derived in Ref. [42]. They are expressed in terms of Wilson-loop operators, convenient for simulations on a discrete space-time lattice. For example, $V_{p^2}^{(2,0)}(r)$ has the form:

$$V_{p^2}^{(2,0)}(r) = \frac{i}{2}\hat{r}^i\hat{r}^j \lim_{T\to\infty}\int_0^T dt\, t^2 \langle\!\langle g\vec{E}_1^i(t) g\vec{E}_1^j(0)\rangle\!\rangle_\Box\,, \quad (5.11)$$

where $\langle\!\langle \ldots \rangle\!\rangle_\Box$ is defined as in Section 4.1. See Ref. [42] for the definition of the other potentials.

5.2 Lattice QCD results

5.2.1 Spin-dependent potentials

The spin-dependent potentials have been studied in lattice QCD simulations by several groups already in the 1980s and 1990s [43, 44, 45, 46, 47]. However, it was observed that these potentials suffer from large numerical errors. The findings indicated that only the spin-orbit potential $V_1'(r)$ has a long-ranged non-perturbative content.

The numerical errors could be reduced in more recent lattice studies by using a new approach [38, 39, 48]. The authors employed the multi-level algorithm for measuring the field strength correlators, analogous to their studies of the $1/m$ potential. The results are shown in Figs. 5.1, 5.2 and suggest that, in addition to $V_1'(r)$, also $V_2'(r)$ contains a finite non-perturbative contribution. There is no indication for a non-perturbative contribution in $V_3(r)$ and $V_4(r)$. Note that a sign of the spin-spin potential $V_4(r)$ as the one shown in Fig. 5.2, would imply a mass ordering of hyperfine multiplets opposite to the ordering observed empirically.

The spin-dependent terms are parametrized in this lattice analysis in terms of $V_1'(r)$, $V_2'(r)$, $V_3(r)$ and $V_4(r)$. This common parametrization has been intro-

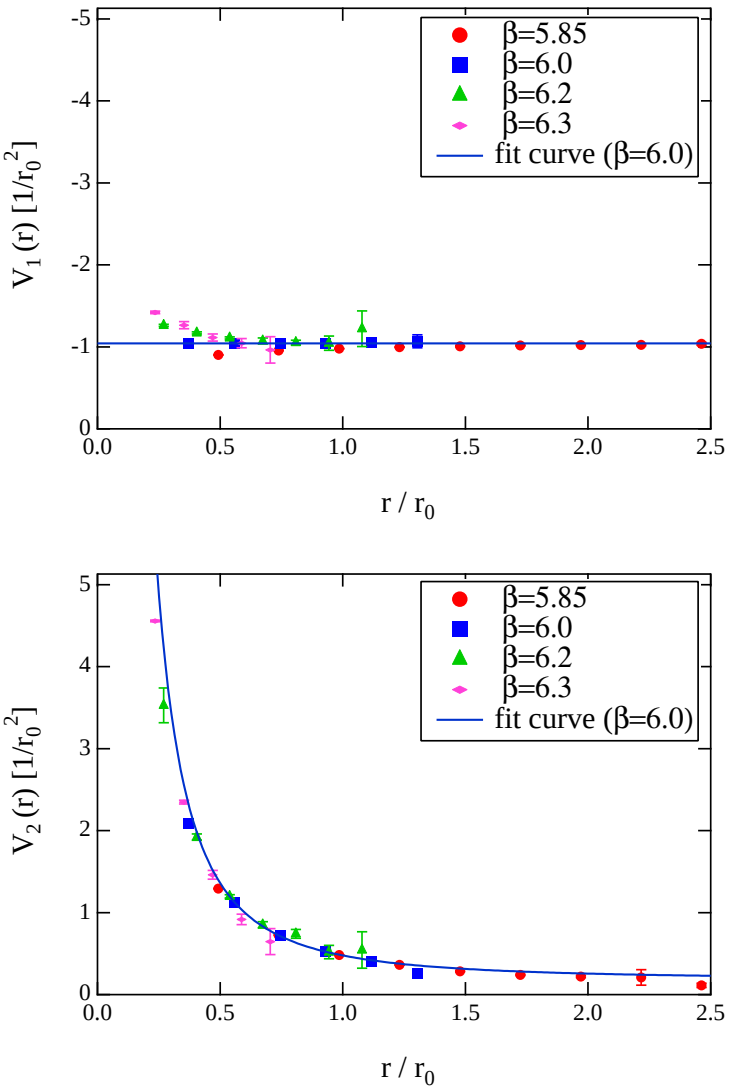

Figure 5.1: Lattice QCD results for the spin-dependent potentials $V_1'(r)$ and $V_2'(r)$ in units of $r_0 \approx 0.5$ fm. Plots are taken from Ref. [48].

duced by Eichten and Feinberg in 1981 [49][1]:

$$V_{\mathrm{SD}}^{(2)}(r) = \left(\frac{\vec{S}_1\cdot\vec{L}_1}{m_1^2} - \frac{\vec{S}_2\cdot\vec{L}_2}{m_2^2}\right)\left(\frac{V^{(0)\prime}(r)}{2r} + \frac{V_1'(r)}{r}\right) + \left(\frac{\vec{S}_2\cdot\vec{L}_1}{m_1 m_2} - \frac{\vec{S}_1\cdot\vec{L}_2}{m_1 m_2}\right)\frac{V_2'(r)}{r} + \frac{1}{m_1 m_2}\left(\frac{(\vec{S}_1\cdot r)(\vec{S}_2\cdot r)}{r^2} - \frac{\vec{S}_1\cdot\vec{S}_2}{3}\right)V_3(r) + \frac{\vec{S}_1\cdot\vec{S}_2}{3m_1 m_2}V_4(r)\,. \tag{5.12}$$

$V^{(0)}(r)$ is the static potential and the prime symbol indicates the derivative with

[1]Note that the potentials $V_3(r)$ and $V_4(r)$ are exchanged with one another compared to Ref. [49].

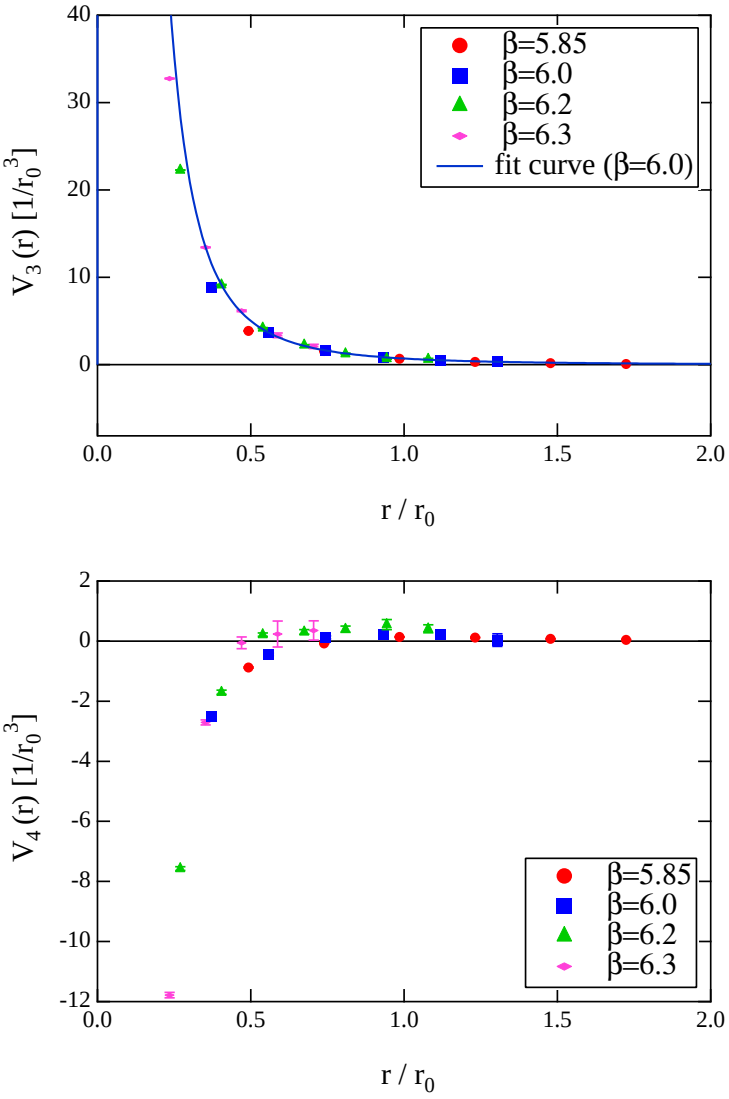

Figure 5.2: Lattice QCD results for the spin-dependent potentials $V_3(r)$ and $V_4(r)$ in units of $r_0 \approx 0.5$ fm. Plots are taken from Ref. [48].

respect to r. This is an alternative parametrization of the spin-dependent potential, previously written in terms of $V_{\rm SD}^{(2,0)}(r)$, $V_{\rm SD}^{(0,2)}(r)$ and $V_{\rm SD}^{(1,1)}(r)$ in Eqs. (5.3), (5.4) and (5.9).

The Gromes relation [50],

$$V^{(0)\prime}(r) = V_2'(r) - V_1'(r)\,, \tag{5.13}$$

is an analytic relation that is derived from Lorentz invariance. It is important to check whether the lattice results are in agreement with this relation or not. As shown in Fig. 5.3, for $\beta = 5.85$ (corresponding to a coarse lattice spacing with $a \approx 0.123$ fm) a deviation from the Gromes relation about 10%-12% is found.

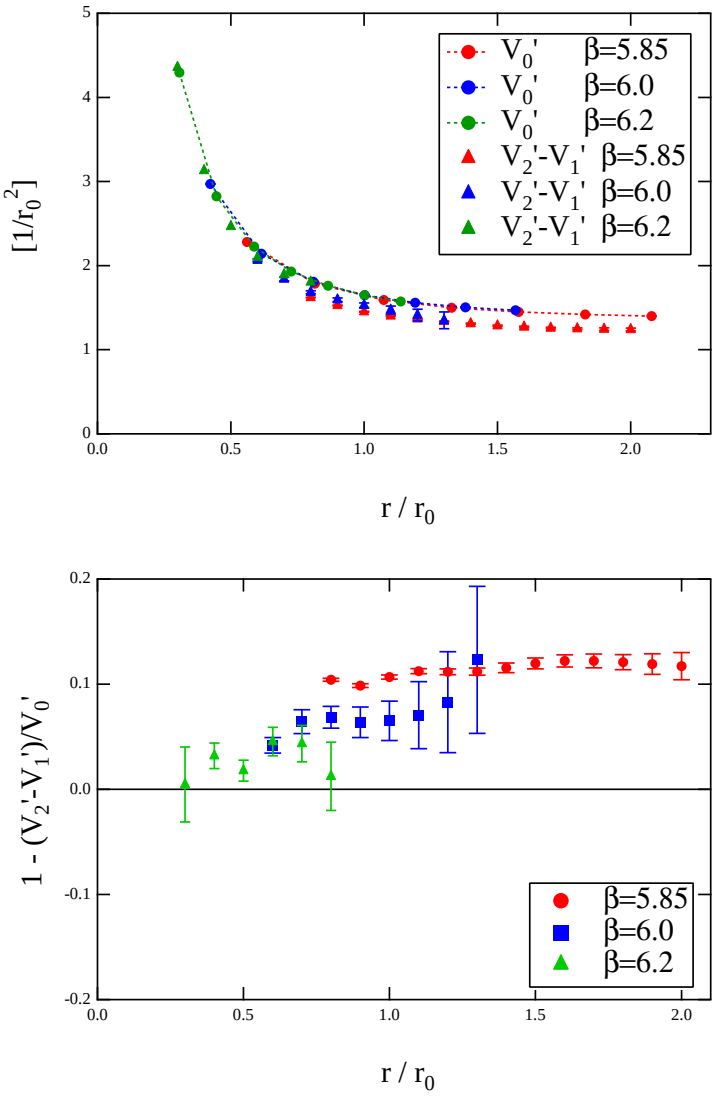

Figure 5.3: Test if the lattice potentials fulfill the Gromes relation (5.13). The absolute deviation and relative deviation from the Gromes relation are shown. Plots are taken from Ref. [48].

One sees a tendency that the deviation decreases for finer lattice spacings. For $\beta = 6.2$ (corresponding to $a \approx 0.068$) one finds a small deviation from the Gromes relation by a few percent.

5.2.2 Spin-independent potentials

In addition to the spin-dependent potentials, the spin-independent potentials have also been studied in lattice simulations by Y. & M. Koma and H. Wittig [51, 48]. They are decomposed in the potentials $V_b(r)$, $V_c(r)$, $V_d(r)$ and $V_e(r)$ which

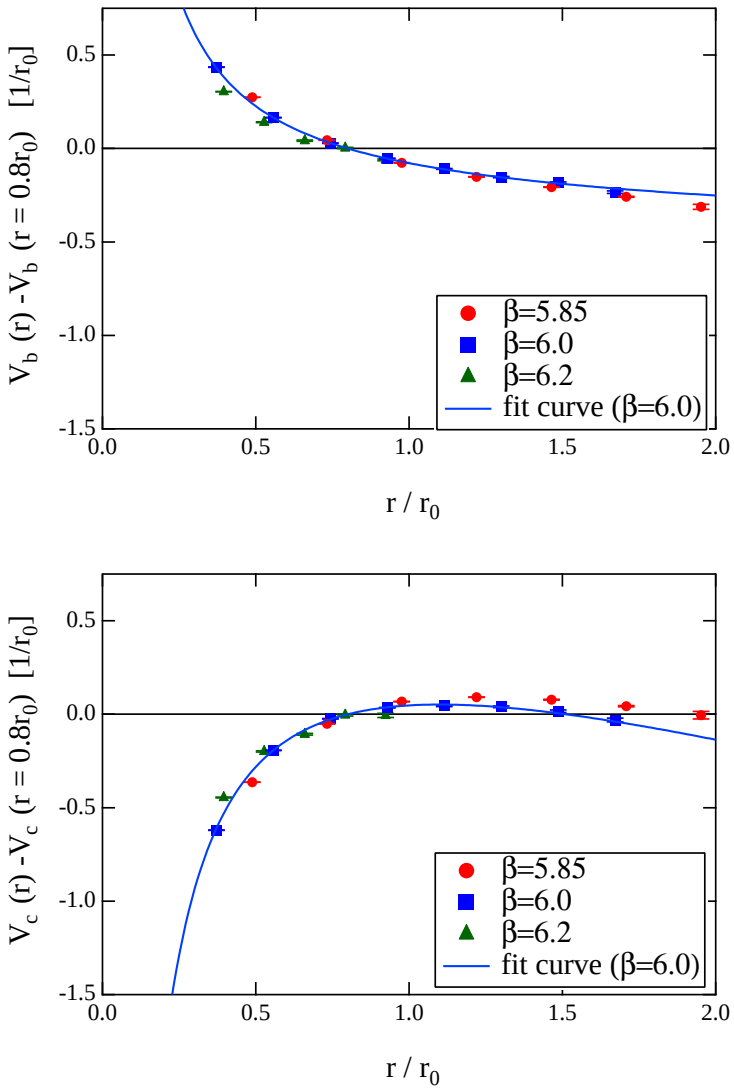

Figure 5.4: Lattice QCD results for the spin-independent potentials $V_b(r)$ and $V_c(r)$ in units of $r_0 \approx 0.5$ fm. Plots are taken from Ref. [48].

have been defined as in Refs. [52, 53] and are related to the potentials introduced in Section 5.1 by:

$$V_{p^2}^{(2,0)}(r) = V_{p^2}^{(0,2)}(r) = V_d(r) - \frac{2}{3}V_e(r)\,, \qquad V_{L^2}^{(2,0)}(r) = V_{L^2}^{(0,2)}(r) = V_e(r)\,,$$
$$V_{p^2}^{(1,1)}(r) = -V_b(r) + \frac{2}{3}V_c(r)\,, \qquad V_{L^2}^{(1,1)}(r) = -V_c(r)\,. \tag{5.14}$$

The lattice results, shown in Figs. 5.4 and 5.5, agree to some extent with

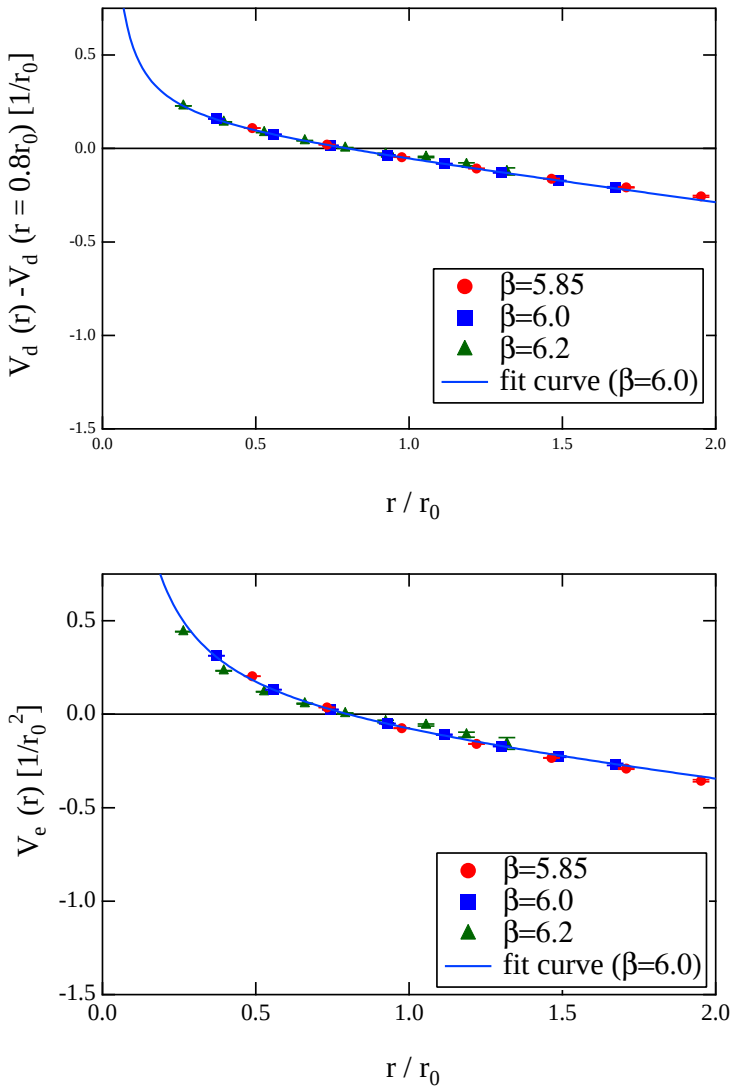

Figure 5.5: Lattice QCD results for the spin-independent potentials $V_d(r)$ and $V_e(r)$ in units of $r_0 \approx 0.5$ fm. Plots are taken from Ref. [48].

estimates that have been derived more than 20 years ago [52]:

$$V_b(r) = \frac{8\,\alpha_s}{9\,r} - \frac{1}{9}\,\sigma\,r\,, \qquad V_c(r) = -\frac{2\,\alpha_s}{3\,r} - \frac{1}{6}\,\sigma\,r\,,$$
$$V_d(r) = -\frac{1}{9}\,\sigma\,r\,, \qquad V_e(r) = -\frac{1}{6}\,\sigma\,r\,, \tag{5.15}$$

where the constant σ represents the string tension of the static potential. The long-range behavior of Eq. (5.15) has been estimated by exploiting an idea of Gromes [50]. The short-range behavior was guessed by neglecting all gluon-gluon interactions. Equation (5.15) combines the estimate for the two different

regions. The lattice result for $V_b(r)$ can be reproduced by setting $\alpha_s \approx 0.25$ and $\sigma \approx 1.0$ GeV/fm, whereas $V_c(r)$ shows better agreement with the lattice potential if one sets $\alpha_s \approx 0.6$ and $\sigma \approx 1.5$ GeV/fm. The observed slope of the long-distance parts of $V_d(r)$ and $V_e(r)$ is reproduced well by $\sigma = 1.5$ GeV/fm.

Note that the spin-independent potentials have been investigated in an earlier lattice study by G. Bali *et al.* [47], however with large statistical errors.

The lattice results can be checked by non-perturbative relations [52, 53] which connect linear combinations of $V_b(r)$, $V_c(r)$, $V_d(r)$, $V_e(r)$ to the static potential. They are often called the BBMP relations:

$$\begin{aligned} V_b(r) + 2\,V_d(r) &= -\frac{1}{2}\,V^{(0)}(r) + \frac{r}{6}\,V^{(0)\prime}(r)\,, \\ V_c(r) + 2\,V_e(r) &= -\frac{r}{2}\,V^{(0)\prime}(r)\,. \end{aligned} \tag{5.16}$$

The authors state in Ref. [51] that the BBMP relations seem to be satisfied, but they find a small discrepancy at short distances and plan a careful investigation of this issue in a future publication.

5.3 Spin-dependent potentials in perturbative QCD

In this section we extend the method used to construct the perturbative potential at leading order and at order $1/m$ and apply it to the spin-dependent potentials at order $1/m^2$. The starting point is again the q-space potential derived within pNRQCD. It reads at leading order for equal masses of the two particles, $m = m_1 = m_2$ [54]:

$$\begin{aligned} \tilde{V}^{(2)}_{\rm SD}(|\vec{q}\,|) &= \frac{4\pi C_F}{m^2}\,\alpha_s(|\vec{q}\,|) \\ &\times \left[\frac{1}{3}(\vec{S}_1+\vec{S}_2)^2 - \left(\frac{(\vec{q}\cdot\vec{S}_1)(\vec{q}\cdot\vec{S}_2)}{\vec{q}^{\,2}} - \frac{\vec{S}_1\cdot\vec{S}_2}{3}\right) + \frac{3i}{2\,\vec{q}^{\,2}}(\vec{S}_1+\vec{S}_2)\cdot(\vec{p}\times\vec{q}\,)\right], \end{aligned} \tag{5.17}$$

where $\vec{p} = \vec{p}_1 = -\vec{p}_2$. The r-space potential is then again defined via a restricted Fourier transformation with the low-momentum cutoff μ_f'':

$$V^{(2)}_{\rm SD}(r,\mu_f'') = \int\limits_{|\vec{q}\,|>\mu_f''} \frac{d^3\vec{q}}{(2\pi)^3}\; e^{i\vec{q}\cdot\vec{r}}\,\tilde{V}^{(2)}_{\rm SD}(|\vec{q}\,|)\,. \tag{5.18}$$

This integral cannot be evaluated numerically in this form due to the tensor structure in $\tilde{V}^{(2)}_{\rm SD}(|\vec{q}\,|)$.

We define the scalar functions A, B and C, again with a low-momentum cutoff μ_f'':

$$A(r,\mu_f'') = \int\limits_{|\vec{q}|>\mu_f''} \frac{d^3\vec{q}}{(2\pi)^3}\, e^{i\vec{q}\cdot\vec{r}}\, \frac{\alpha_s(|\vec{q}|)\,(\vec{q}\cdot\vec{r})}{i\,\vec{q}^{\,2}}\,, \tag{5.19}$$

$$B(r,\mu_f'') = \int\limits_{|\vec{q}|>\mu_f''} \frac{d^3\vec{q}}{(2\pi)^3}\, e^{i\vec{q}\cdot\vec{r}}\, \alpha_s(|\vec{q}|)\,, \tag{5.20}$$

$$C(r,\mu_f'') = \int\limits_{|\vec{q}|>\mu_f''} \frac{d^3\vec{q}}{(2\pi)^3}\, e^{i\vec{q}\cdot\vec{r}}\, \frac{\alpha_s(|\vec{q}|)\,(\vec{q}\cdot\vec{r})^2}{\vec{q}^{\,2}}\,. \tag{5.21}$$

These functions can be handled numerically[2] and are illustrated in Fig. 5.6. One observes significant deviations from corresponding functions where α_s has been set to a constant.

The spin-dependent potential in coordinate space $V_{\rm SD}^{(2)}(r,\mu_f'')$ can now be expressed in terms of these three scalar functions A, B and C:

$$\begin{aligned} V_{\rm SD}^{(2)}(r,\mu_f'') &= \int\limits_{|\vec{q}|>\mu_f''} \frac{d^3\vec{q}}{(2\pi)^3}\; e^{i\vec{q}\cdot\vec{r}}\, \tilde{V}_{\rm SD}^{(2)}(|\vec{q}|) \\ &= \frac{4\pi C_F}{m^2}\left[2B\frac{\vec{S}_1\cdot\vec{S}_2}{3}+\left(\frac{B}{2}-\frac{3C}{2r^2}\right)\left(\frac{(\vec{S}_1\cdot\vec{r})(\vec{S}_2\cdot\vec{r})}{r^2}-\frac{\vec{S}_1\cdot\vec{S}_2}{3}\right)+\frac{3A}{2r^2}\vec{L}_1\cdot(\vec{S}_1+\vec{S}_2)\right]. \end{aligned} \tag{5.22}$$

The same structure of spin-dependent terms as in the parametrization by Eichten and Feinberg (see Eq. (5.12)) appears here. This allows for a comparison with the lattice QCD potentials.

The coefficient of the spin-orbit term in Eq. (5.12) becomes proportional to $3V_2'(r) + V_1'(r)$ for equal masses and after making use of the Gromes relation. By comparing it to the spin-orbit term in Eq. (5.22) one finds the following correspondence:

$$3\,V_2'(r) + V_1'(r) \;\to\; \frac{16\,\pi A}{r}\,. \tag{5.23}$$

A comparable slope over quite a large range, even at distances where perturbation theory is not expected to work, is found (see Fig. 5.7).

By comparing of the coefficients of the tensor and spin-spin term of the two different parametrizations one finds the correspondences:

$$V_3(r) \;\to\; \frac{8\,\pi}{3}\left(B-\frac{3\,C}{r^2}\right), \tag{5.24}$$

$$V_4(r) \;\to\; \frac{32\,\pi B}{3}\,. \tag{5.25}$$

[2]The integral in Eq. (5.20) can be carried out after rewriting it as in Eq. (6.14) in Section 6.3.

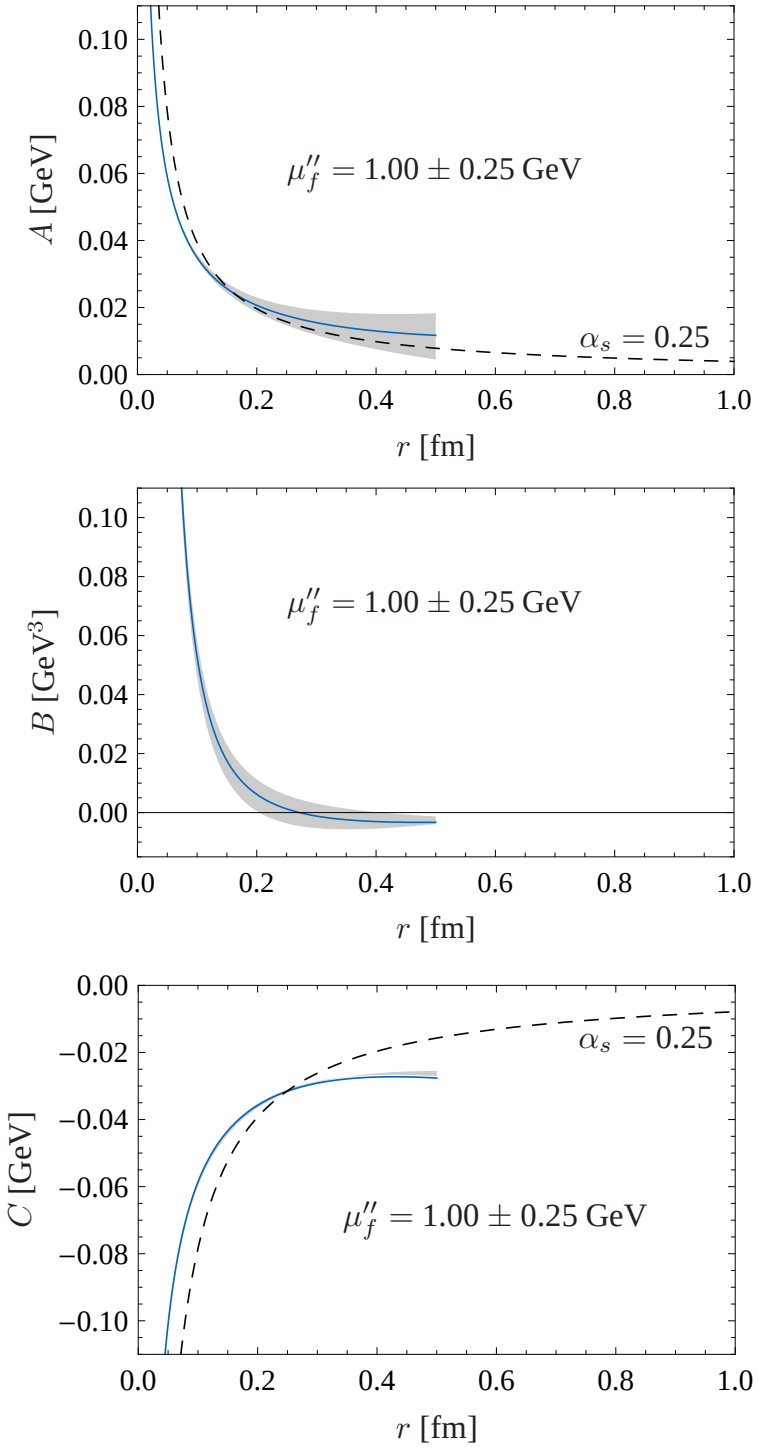

Figure 5.6: Numerical results for the functions $A(r, \mu_f'')$, $B(r, \mu_f'')$ and $C(r, \mu_f'')$. The functions A and C, which include the full RG running of $\alpha_s(|\vec{q}|)$, are compared to corresponding functions where the strong coupling has been set to the constant value $\alpha_s = 0.25$. A constant α_s in B gives a result proportional to the δ-function.

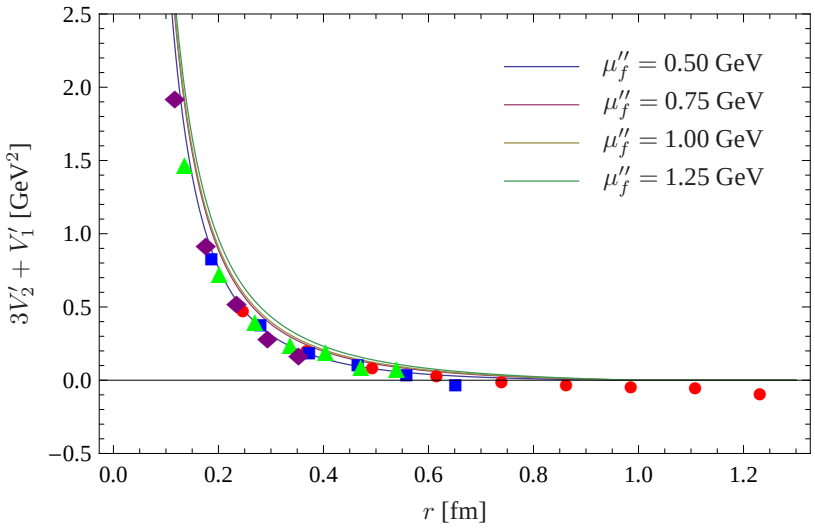

Figure 5.7: Comparison of the perturbative spin-orbit term (for different values of μ_f'') with lattice QCD results [48].

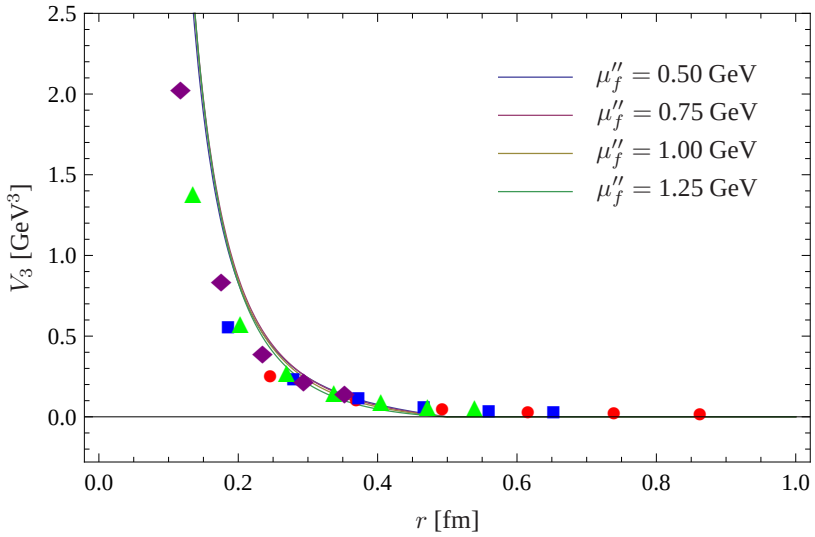

Figure 5.8: Comparison of the perturbative tensor term (for different values of μ_f'') with lattice QCD results [48].

Figure 5.8 compares the tensor term from lattice simulations to the one from our perturbative construction. The agreement is not as good as for the spin-orbit term. Finally, no agreement is found for the spin-spin term (see Fig. 5.9) where the lattice QCD result appears to have a sign that contradicts standard expectations from spectroscopy. We shall return to this issue in the next chapter.

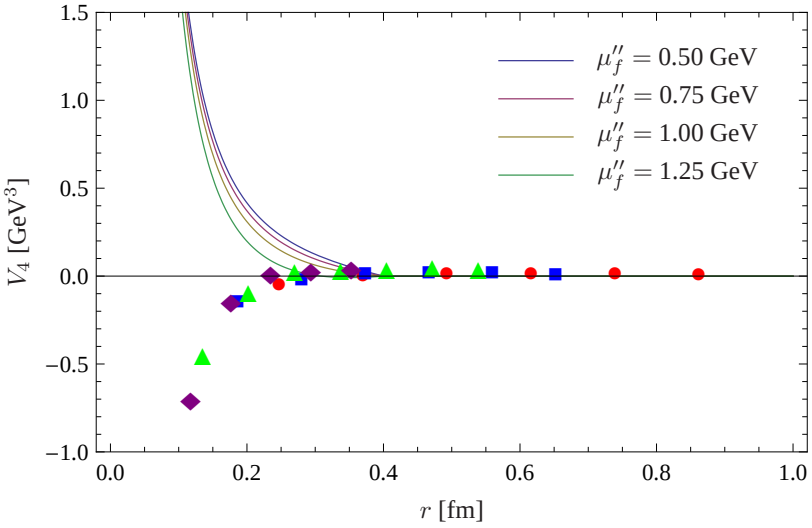

Figure 5.9: Comparison of the perturbative spin-spin term (for different values of μ_f'') with lattice QCD results [48].

6 Matching to a new lattice QCD approach

6.1 Charmonium potentials in full lattice QCD

A new lattice QCD approach to extract the heavy-quark potentials has been proposed in Ref. [55]. The spin-spin and central potentials at finite quark mass are obtained from Nambu-Bethe-Salpeter (NBS) amplitudes through an effective Schrödinger equation. A high precision analysis in "full QCD", with the focus on charmonium, has been performed in a subsequent analysis [56]. Tensor and spin-orbit terms will not be discussed in this chapter. These have so far not been studied in the new lattice QCD approach employing the NBS amplitudes.

In order to obtain the potentials, the NBS wave function $\phi_\Gamma(\vec{r})$ is extracted in lattice simulations from four-point correlation functions:

$$\phi_\Gamma(\vec{r}) = \sum_{\vec{x}} \left\langle 0 \middle| \overline{Q}(\vec{x})\Gamma Q(\vec{x}+\vec{r}) \middle| Q\overline{Q}; J^{PC} \right\rangle , \tag{6.1}$$

where $\vec{r}$ is again the relative coordinate of the two quarks and Γ is any of the 16 Dirac γ matrices. For the vector channel ($J^{PC} = 1^{--}$) Γ is chosen as γ_i, for the pseudoscalar channel ($J^{PC} = 0^{-+}$) Γ is chosen as γ_5. In the case of S-wave charmonium states (i.e., without tensor and spin-orbit terms), the stationary Schrödinger equation for the NBS wave function is reduced to:

$$\left(-\frac{\nabla^2}{m_Q} + V_C(r) + \vec{S}_1 \cdot \vec{S}_2 \, V_S(r) \right) \phi_\Gamma(r) = E_\Gamma \, \phi_\Gamma(r) \, , \tag{6.2}$$

with a central potential $V_C(r)$ and a spin-spin potential $V_S(r)$. The spin operator $\vec{S}_1 \cdot \vec{S}_2$ is substituted with $1/4$ for the vector channel and with $-3/4$ for the pseudoscalar channel. This allows for a separation of the central, spin-independent potential and the spin-spin potential through a linear combination:

$$V_C(r) = \text{const} + \frac{1}{m_Q} \left(\frac{3}{4} \frac{\nabla^2 \phi_{\rm V}(r)}{\phi_{\rm V}(r)} + \frac{1}{4} \frac{\nabla^2 \phi_{\rm PS}(r)}{\phi_{\rm PS}(r)} \right) , \tag{6.3}$$

$$V_S(r) = \Delta E_{\rm hyp} + \frac{1}{m_Q} \left(\frac{\nabla^2 \phi_{\rm V}(r)}{\phi_{\rm V}(r)} - \frac{\nabla^2 \phi_{\rm PS}(r)}{\phi_{\rm PS}(r)} \right) , \tag{6.4}$$

where $\Delta E_{\rm hyp} = M_{\rm V} - M_{\rm PS}$ denotes the mass deference between the vector and pseudoscalar states. The kinetic quark mass m_Q can be obtained by assuming that there is no long-range correlation and no (irrelevant) constant term in the spin-spin potential. From $\lim_{r\to\infty} V_S(r) = 0$ follows:

$$m_Q = \lim_{r\to\infty} \frac{-1}{\Delta E_{\rm hyp}} \left(\frac{\nabla^2 \phi_{\rm V}(r)}{\phi_{\rm V}(r)} - \frac{\nabla^2 \phi_{\rm PS}(r)}{\phi_{\rm PS}(r)} \right) . \tag{6.5}$$

The central potential includes charm-quark mass effects to all orders and is shown in Fig. 6.1. It can be fitted well by the Cornell parametrization,

$$V_C^{\rm lat}(r) = -\frac{A}{r} + \sigma\, r + {\rm const}\,, \tag{6.6}$$

with $A = 0.813 \pm 0.022$ and $\sqrt{\sigma} = (0.394 \pm 0.007)$ GeV.

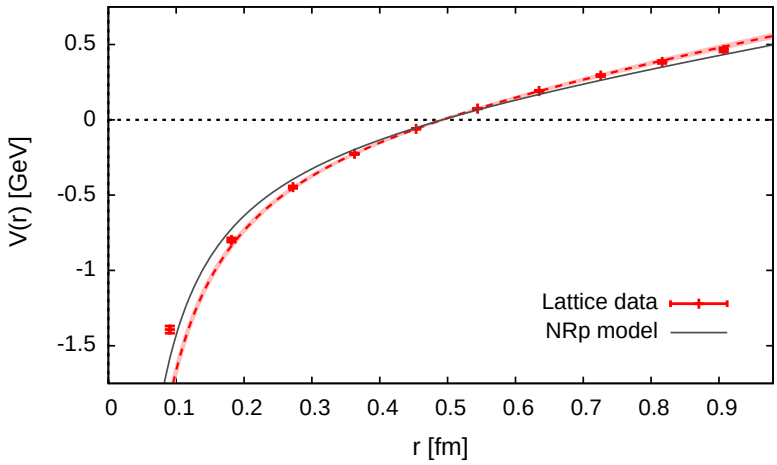

Figure 6.1: Spin-independent charmonium potential calculated from the NBS wave function. For comparison, a phenomenological potential [57] is shown (solid curve). Plot is taken from Ref. [56].

A repulsive spin-spin potential (see Fig. 6.2) which shifts spin-triplet states upward and spin-singlet states downward is found in this new lattice approach, as required for reproducing the experimental charmonium and bottomonium spectra. The resulting shape of the potential is quite different from a δ-function potential that one commonly obtains from one-gluon exchange with an effective coupling strength α_s treated as an adjustable parameter. The spin-spin potential is fitted in Ref. [56] with three different functional forms: i.e., Yukawa, exponential and Gaussian parametrization. The exponential form provides the best fit to the lattice data and reads,

$$V_S^{\rm lat}(r) = \alpha\, e^{-\beta r}\,, \tag{6.7}$$

with $\alpha = (0.825 \pm 0.019)$ GeV and $\beta = (1.982 \pm 0.024)$ GeV.

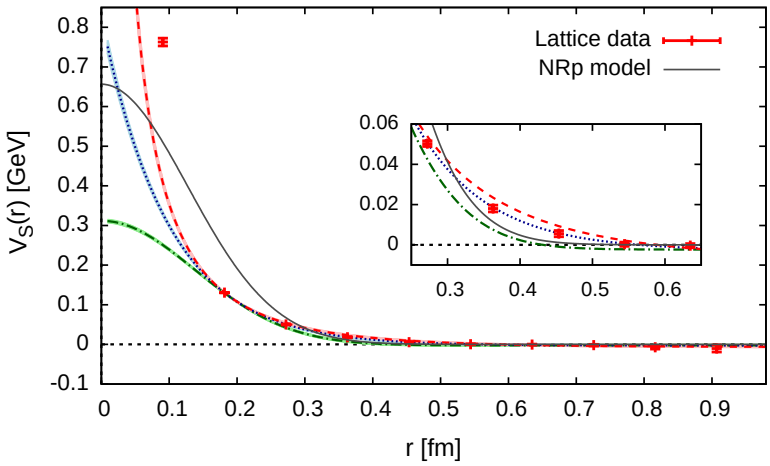

Figure 6.2: Spin-spin charmonium potential calculated from the NBS wave function. Different fits curves and a phenomenological potential [57] (solid curve) are shown. Plot is taken from Ref. [56].

6.2 Central charmonium potential

In this section we consider the perturbative central (spin-independent) charmonium potential. As before, it as defined in r-space via a restricted Fourier transformation with a low-momentum cutoff μ_C:

$$V_C^{\rm pert}(r,\mu_C) = \int\limits_{q>\mu_C} \frac{d^3q}{(2\pi)^3}\, e^{i\vec{q}\cdot\vec{r}} \left[\tilde{V}^{(0)}(q) + \frac{\tilde{V}^{(1)}(q)}{m/2}\right], \tag{6.8}$$

with $q = |\vec{q}|$. The static potential $\tilde{V}^{(0)}(q)$ will be used at two-loop order in momentum space

$$\tilde{V}^{(0)}(q) = -\frac{16\pi\alpha_s(q)}{3q^2}\left[1 + \frac{\alpha_s(q)}{4\pi}\,a_1 + \frac{\alpha_s^2(q)}{(4\pi)^2}\,a_2\right], \tag{6.9}$$

and the $1/m$ potential at leading order [32]:

$$\tilde{V}^{(1)}(q) = -\frac{2\pi^2\alpha_s^2(q)}{q}\,. \tag{6.10}$$

The low-momentum region, not accessible in perturbation theory, is excluded in Eq. (6.8). In contrast to Chapters 3 and 4, a single cutoff value μ_C is used for the sum of the static potential and the $1/m$ potential [58]. Again full four-loop renormalization-group (RG) running for the strong coupling $\alpha_s(q)$, here with three light flavors, is understood.

The perturbative potential is matched at a suitable distance $r_m = 0.14$ fm to the spin-independent potential calculated in full lattice QCD (see previous

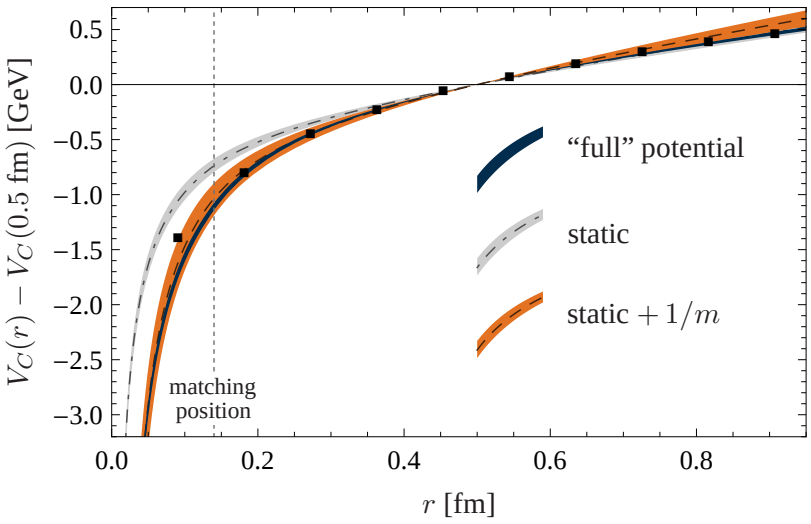

Figure 6.3: Charmonium potential from a combination of perturbative QCD and lattice QCD [56] matched at $r_m = 0.14$ fm (solid curve). The dot-dashed line (with error band) shows the static potential from Chapter 3 for comparison, while the dashed line (with error band) shows the static-plus-$1/m$ potential from Chapter 4. The energy scale is chosen relative to the potential at $r = 0.5$ fm for convenience.

section). In the region around $r_m = 0.14$ fm, the perturbative potential and the lattice potential are both expected to be reliable. The potential changes only marginally under limited variations of the matching point. Optimal matching is achieved with a low-momentum cutoff $\mu_C = (0.54 \pm 0.02)$ GeV.

In Fig. 6.3 we compare this matched central potential (solid curve) with the potential obtained in the Wilson-loop approach using a $1/m$ expansion. One observes that the "full" potential differs significantly from the static potential (dot-dashed line with error band), but it is consistent within errors when the $1/m$ potential is added to the static potential (dashed line with error band). The charm-quark mass m relevant for the $1/m$ potential has been varied in Fig. 6.3 in the range (1.5 ± 0.2) GeV.

6.3 Spin-spin potential for charmonium

In the following we construct a perturbative spin-spin potential that can be used to continue the lattice spin-spin potential to short distances. Recall first the well-known (schematic) spin-spin potential derived from one-gluon exchange assuming a constant coupling α_s:

$$V_S(r) = \frac{32\pi}{9m_q^2}\,\alpha_s\,\delta^3(\vec{r})\,, \tag{6.11}$$

with the quark/antiquark mass m_q. This δ-function term is in agreement with the leading-order spin-spin potential obtained in pNRQCD [59].

It is possible to include the RG running of $\alpha_s(q)$ in the construction of the spin-spin potential (see also Chapter 5). We define the perturbative part of $V_S(r)$ here as:

$$V_S^{\rm pert}(r,\mu_S) = \frac{32\pi}{9m^2} \int\limits_{q>\mu_S} \frac{d^3q}{(2\pi)^3}\; e^{i\vec{q}\cdot\vec{r}}\alpha_s(q)\,, \tag{6.12}$$

with a low-momentum cutoff μ_S. For $q > \mu_S$ the perturbative RG evolution of $\alpha_s(q)$ is supposed to be reliable. The non-perturbative infrared behavior of the quark and gluon couplings prohibits a controlled low-momentum extension for $q < \mu_S$. It is nevertheless useful to examine such an extension for $r \ll 1/\mu_S$ in the form

$$V_S^{\rm ir} = \frac{32\pi}{9m^2}\,\overline{\alpha}_s \int\limits_{q<\mu_S} \frac{d^3q}{(2\pi)^3}\, e^{i\vec{q}\cdot\vec{r}} \simeq \frac{16\,\overline{\alpha}_s}{27\pi m^2}\,\mu_S^3\,, \tag{6.13}$$

with a parameter $\overline{\alpha}_s$ reflecting the average interaction strength in the infrared region. Note that Eq. (6.13) gives a positive constant proportional to μ_S^3 to be added as a correction to $V_S^{\rm pert}(r,\mu_S)$, with $\overline{\alpha}_s$ not known, but expected to be of $\mathcal{O}(1)$.

In order to facilitate the numerical evaluation of the Fourier integral for the perturbative part, it is useful to rewrite $V_S^{\rm pert}(r,\mu_S)$ in the form

$$V_S^{\rm pert}(r,\mu_S) = -\frac{16}{9m^2\pi r}\,\frac{\partial}{\partial r} \int\limits_{\mu_S}^{\infty} dq\,\cos(qr)\,\alpha_s(q)\,. \tag{6.14}$$

To be consistent with the lattice QCD analysis, the charm-quark mass m in the denominator of Eq. (6.14) is identified with $m_Q = (1.74 \pm 0.03)$ GeV, the kinetic quark mass that has been determined in Ref. [56]. Discarding the additive constant $V_S^{\rm ir}$ in the first step, the resulting short distance potential and its dependence on the cutoff scale μ_S is shown in Fig. 6.4. The shape is evidently very different from a Gaussian or a δ-function. Such forms are frequently used for the spin-spin potential in phenomenological models.

The two components of the spin-spin potential, arising from perturbative QCD for $r \le r_m$ and from lattice QCD for $r \ge r_m$ (see Section 6.1), can be matched at $r_m = 0.14$ fm. When ignoring the additive constant $V_S^{\rm ir}$ this matching is achieved for $\mu_S = (0.43 \pm 0.02)$ GeV. With inclusion of the (variable) additive constant $V_S^{\rm ir}$ the infrared cutoff μ_S can be varied over a wide range almost without any effect on the spin-spin potential. Figure 6.5 shows the matched potential with an infrared cutoff of $\mu_S = (0.75 \pm 0.25)$ GeV.

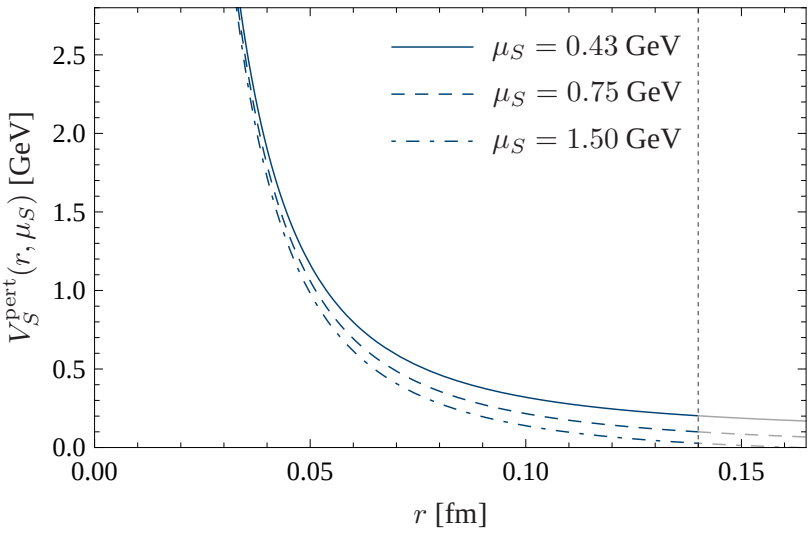

Figure 6.4: Spin-spin potential in r-space derived from one-gluon exchange as defined in Eq. (6.14). The potential is shown for different values of the low-momentum cutoff μ_S.

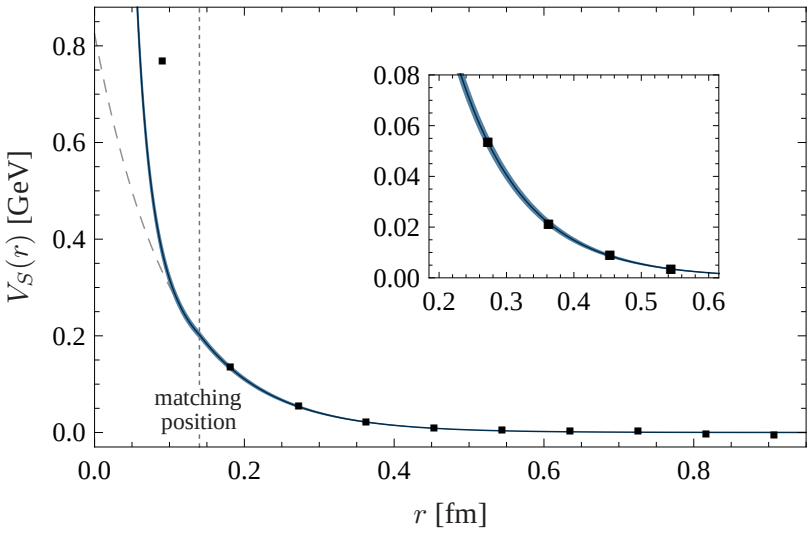

Figure 6.5: Charmonium spin-spin potential (with error band) from a combination of perturbative QCD (see Eq. (6.14)) and lattice QCD [56], matched at $r_m = 0.14$ fm. Dashed line: continuation of the exponential lattice fit (6.7) to short distances.

7 Spectroscopy and extraction of quark masses

7.1 Static potential

7.1.1 Leading-order results for quarkonium spectra

For first orientation we consider the bottomonium and charmonium spectrum from the leading order QCD potential. The Schrödinger equation with the matched static potential, derived in Chapter 3, is solved numerically:

$$\left[-\frac{1}{m}\vec{\nabla}^2 + 2m_{\rm PS}(\mu_f) + V^{(0)}(r,\mu_f) - E \right]\psi(\vec{r}) = 0\,. \tag{7.1}$$

The heavy-quark mass m appearing in the denominator of the kinetic energy is not *a priori* determined. In practice we use values close to the static $\overline{\rm MS}$ masses: $m = 4.2$ GeV for bottomonium and $m = 1.25$ GeV for charmonium. Small variations from these values do not have any significant influence on the results.

The single free parameter in the Schrödinger equation is the potential-subtracted (PS) quark mass $m_{\rm PS}(\mu_f)$, to be defined in Section 7.1.2. Modifications of this parameter cause a constant shift of all states. In the case of bottomonium we fix it by the choice to reproduce the measured $\Upsilon(2S)$ energy and find the value $m_{\rm PS}(\mu_f = 0.908\ {\rm GeV}) = 4.78$ GeV. The scale $\mu_f = 0.908$ GeV was obtained in Chapter 3 and will be important for the translation of the PS mass into the bottom quark mass defined in other schemes.

The resulting bottomonium spectrum, without accounting for any spin effects, is shown in Fig. 7.1. Most of the measured states are already roughly reproduced in this first approach. The largest deviations from experiment are observed for the two lowest states $\eta_{\rm b}(1S)$ and $\Upsilon(1S)$. For guidance, also $\eta_{\rm b}(2S)$ has been included. First evidence for this state has been reported recently in Refs. [60, 61].

In the charmonium case we fit to the $\rm h_c(1P)$ energy and find $m_{\rm PS}(\mu_f = 0.930\ {\rm GeV}) = 1.39$ GeV (see Fig. 7.2).

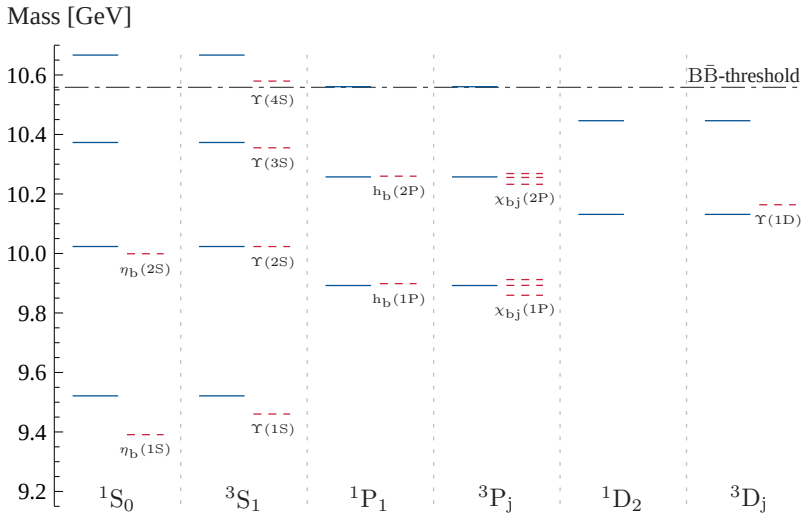

Figure 7.1: Bottomonium spectrum. Model predictions based on the static potential (solid lines) are compared to states observed in experiment (dashed lines).

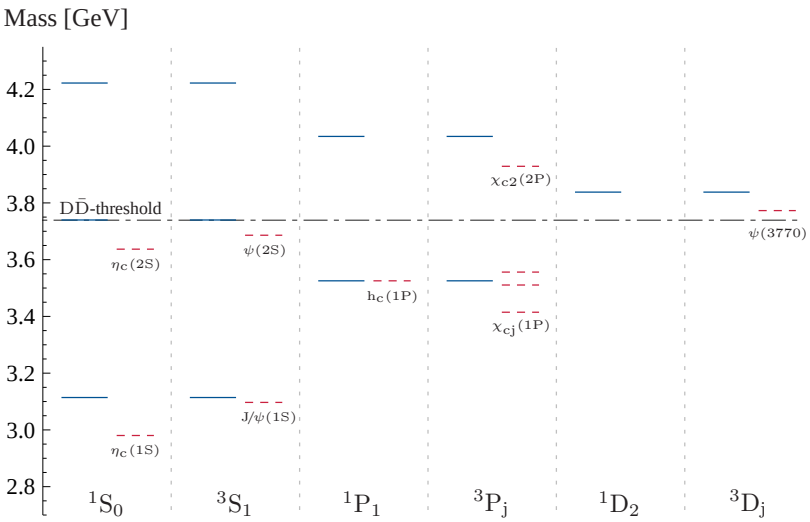

Figure 7.2: Charmonium spectrum. Model predictions based on the static potential (solid lines) are compared to states observed in experiment (dashed lines).

7.1.2 Extraction of charm- and bottom-quark masses

The scale-dependent PS mass is defined as [12]:

$$m_{\mathrm{PS}}(\mu_f) = m_{\mathrm{pole}} + \frac{1}{2}\int\limits_{|\vec{q}|<\mu_f} \frac{d^3q}{(2\pi)^3}\,\tilde{V}^{(0)}(|\vec{q}\,|) = m_{\mathrm{pole}} + \frac{1}{4\pi^2}\int\limits_0^{\mu_f} dq\, q^2\,\tilde{V}^{(0)}(q)\,. \quad (7.2)$$

This $m_{\rm PS}$ absorbs the unknown additive constant of the potential and is free from the leading renormalon ambiguity [12, 13].

To convert the PS mass to the mass in the more commonly used $\overline{\rm MS}$ scheme, it is necessary to introduce the pole mass $m_{\rm pole}$ as an intermediate step. The relation between $m_{\rm pole}$ and $m_{\rm PS}$ reads [12]:

$$m_{\rm pole} = m_{\rm PS}(\mu_f) + \frac{C_F\,\alpha_s(\mu)\,\mu_f}{\pi}\left\{1 + \frac{\alpha_s(\mu)}{4\pi}\left[a_1 - \beta_0\left(\ln\frac{\mu_f^2}{\mu^2} - 2\right)\right]\right.$$
$$\left. + \left(\frac{\alpha_s(\mu)}{4\pi}\right)^2\left[a_2 - (2a_1\beta_0 + \beta_1)\left(\ln\frac{\mu_f^2}{\mu^2} - 2\right) + \beta_0^2\left(\ln^2\frac{\mu_f^2}{\mu^2} - 4\ln\frac{\mu_f^2}{\mu^2} + 8\right)\right] + \mathcal{O}(\alpha_s^3)\right\}. \tag{7.3}$$

The same conventions as in the Section 3.2 and the Appendix A.1 are used. Note that a renormalization scale μ appears in the coupling. In the following μ is set equal to the $\overline{\rm MS}$ mass $\overline{m} \equiv m_{\overline{\rm MS}}(m_{\overline{\rm MS}})$. This $\overline{m}$ is not known at that point and has to be computed iteratively. In a second step the pole mass is converted to the $\overline{\rm MS}$ mass [62, 63, 64]:

$$\frac{m_{\rm pole}}{\overline{m}} = 1 + \frac{4}{3}\left(\frac{\alpha_s(\overline{m})}{\pi}\right) + \left(\frac{\alpha_s(\overline{m})}{\pi}\right)^2(-1.0414\,n_f + 13.4434)$$
$$+ \left(\frac{\alpha_s(\overline{m})}{\pi}\right)^3(0.6527\,n_f^2 - 26.655\,n_f + 190.595) + \mathcal{O}(\alpha_s^4)\,. \tag{7.4}$$

Note that both relations (7.3) and (7.4), taken individually, show a poorly convergent behavior whereas the relation between $m_{\rm PS}(\mu_f)$ and $\overline{m}$ is expected to be stable. This is in fact confirmed numerically. Using $\mu_f = 0.908$ GeV (from Chapter 3) one obtains the value $\overline{m}_{\rm b} = 4.27$ GeV for the bottom quark. From an analogous translation with $\mu_f = 0.930$ GeV one finds $\overline{m}_{\rm c} = 1.24$ GeV for the charm quark.

However, as shown in Fig. 7.3, the μ_f dependence of $m_{\rm PS}(\mu_f)$ (Eq. (7.3)) differs for $\mu_f \ll \overline{m}$ from the μ_f dependence coming from variations of the cutoff in the numerical integral (solid line). Instead of matching at $\mu_f = 0.908$ GeV it is obviously preferable to use the numerical μ_f dependence first to translate $m_{\rm PS}(\mu_f)$ into $m_{\rm PS}(\overline{m})$ and then apply Eqs. (7.3) and (7.4) to translate this value into the $\overline{\rm MS}$ scheme. By this method the extraction of $\overline{m}$ becomes independent of the value of μ_f used in the construction of the potential. This leads to improved mass values, $\overline{m}_{\rm b} = 4.20$ GeV for the bottom quark and $\overline{m}_{\rm c} = 1.23$ GeV for the charm quark in the $\overline{\rm MS}$ scheme.

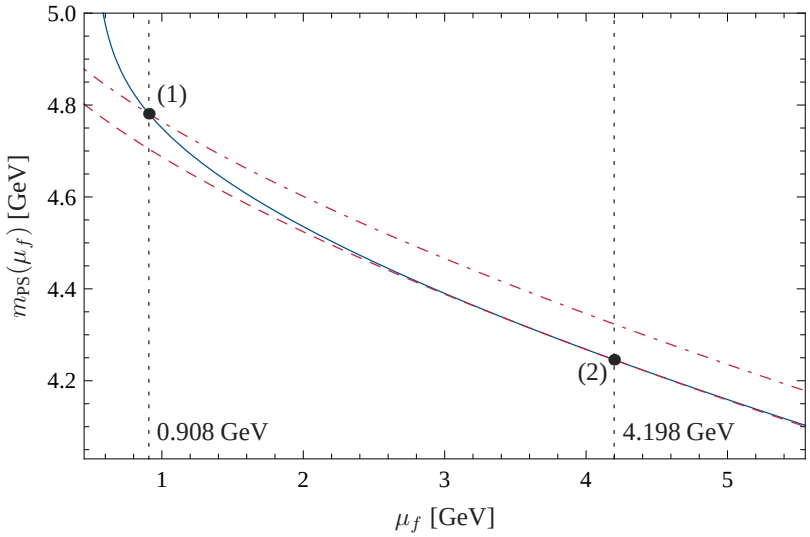

Figure 7.3: Scale dependence of $m_{\rm PS}(\mu_f)$ for the bottomonium case. The solid curve shows the numerical μ_f dependence from Eq. (7.2). The dashed and dashed-dotted curves show the μ_f dependence given by Eq. (7.3) at different matching points. Point (2) is preferred to point (1) for the determination of $\overline{m}_{\rm b}$.

7.2 Analysis at order $1/m$

7.2.1 Quarkonium spectroscopy

Given the potential $V = V^{(0)} + 2\,V^{(1)}/m$ up to order $1/m$ in the heavy-quark mass, we can examine the resulting bottomonium and charmonium spectra, with focus on the effects of the $1/m$ term. The Schrödinger equation at order $1/m$,

$$\left[-\frac{1}{m}\vec{\nabla}^2 + 2m_{\widehat{\rm PS}}(\mu_f,\mu_f') + V^{(0)}(r,\mu_f) + \frac{2}{m}V^{(1)}(r,\mu_f') - E \right]\psi(\vec{r}) = 0\,, \quad (7.5)$$

is solved with the fixed values for μ_f and μ_f' as derived in the construction of the potentials in the Chapters 3 and 4. The potential-subtracted mass $m_{\widehat{\rm PS}}(\mu_f,\mu_f')$ at order $1/m$, to be defined and discussed in detail in the next subsection, is the only free parameter. It sets the overall energy scale and will be fixed by comparison with the measured bottomonium and charmonium spectrum.

Consider now first the bottomonium spectrum below $\rm B\overline{B}$ threshold[1] (see Fig. 7.4). One option is, as before, to fix $m_{\widehat{\rm PS}}(\mu_f,\mu_f')$ such that the measured $\Upsilon(2{\rm S})$ energy is reproduced. Alternatively, the center of the $\chi_{\rm b}(1{\rm P})$ triplet could be used for calibration. These states remain almost unchanged by the $1/m$ effects. The more tightly bound $\eta_{\rm b}(1{\rm S})$ and $\Upsilon(1{\rm S})$ states respond, as expected, more sensitively to the corrections induced by $V^{(1)}(r)$.

[1]Above the $\rm B\overline{B}$ threshold the $\rm b\overline{b}$ potential develops an imaginary part and the present strategy (including lattice QCD) does not apply.

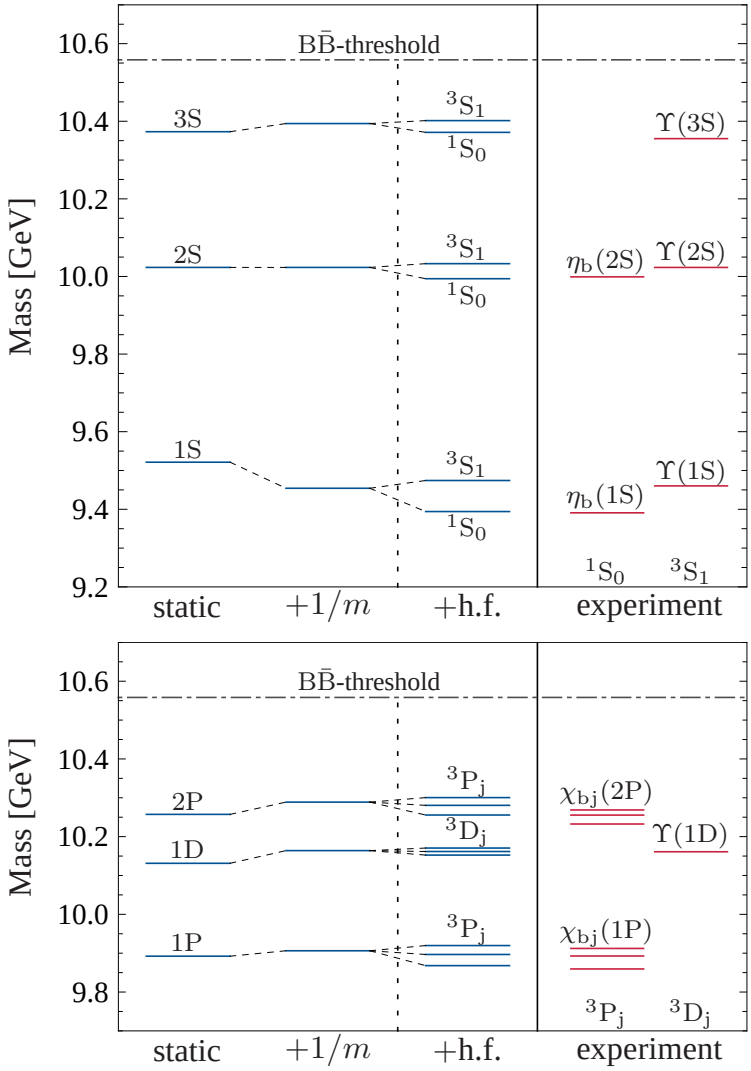

Figure 7.4: Bottomonium spectrum in comparison with experiment. Static plus order $1/m$ results are shown on the left, with additional hyperfine effects (h.f.) added phenomenologically using Eq. (7.6).

An additional effective spin-dependent term from one-gluon exchange (see Appendix A.3),

$$\delta V_{\text{spin}} = \frac{8\pi\alpha_s^{\text{eff}}}{9m^2}(\vec{\sigma}_1\cdot\vec{\sigma}_2)\,\delta^{(3)}(\vec{r}) + \frac{\alpha_s^{\text{eff}}}{m^2}\left(\frac{(\vec{\sigma}_1\cdot\vec{r})(\vec{\sigma}_2\cdot\vec{r})}{r^5} - \frac{\vec{\sigma}_1\cdot\vec{\sigma}_2}{3\,r^3}\right) + \frac{\alpha_s^{\text{eff}}}{m^2}\left(\frac{\vec{L}\cdot\vec{\sigma}_1 + \vec{L}\cdot\vec{\sigma}_2}{r^3}\right), \quad (7.6)$$

with $\alpha_s^{\text{eff}} = 0.3$ can be used to move all states well into their observed positions. For this purpose we replace the delta function (that is exclusively sensitive to

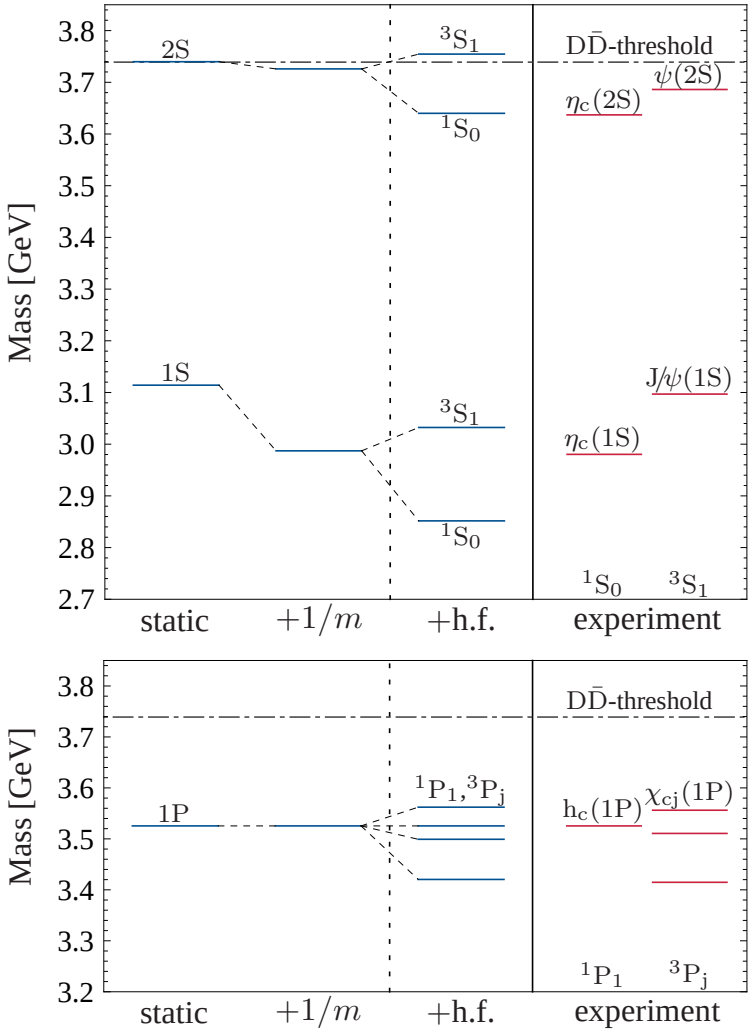

Figure 7.5: Charmonium spectrum in comparison with experiment. Static plus order $1/m$ results are shown on the left, with additional hyperfine effects (h.f.) added phenomenologically.

the wave function at $r = 0$) by a Gaussian distribution

$$\delta^{(3)}(\vec{r}) \to \frac{1}{(\sqrt{\pi}\,\sigma)^3}\, e^{-r^2/\sigma^2}, \tag{7.7}$$

with $\sigma = 0.03$ fm.

As expected, the influence of the $1/m$ term in the potential is much stronger for charmonium (see Fig. 7.5) than for bottomonium. For charmonium we choose the potential-subtracted mass in Eq. (7.5) (reflecting the unknown constants in $V^{(0)}$ and $V^{(1)}$) such that the measured $h_c(1P)$ energy is reproduced also at order $1/m$. With this choice, however, the $V^{(1)}$ part produces a downward shift of 127 MeV in the 1S states ($\eta_c(1S)$ and J/ψ) relative to the static result. This shift is too large in comparison with the measured η_c and J/ψ energies.

The 1S states are naturally more sensitive to $1/m$ corrections than 1P and 2S states because of the leading $1/r^2$ short-distance behavior of $V^{(1)}$. Hence the large shift of the 1S energy level at order $1/m$ does not come unexpectedly. It is nevertheless evident that, no matter which choice is adopted for adjusting the unknown constant in $V^{(1)}$, the 1S and 1P states of charmonium cannot be simultaneously reproduced at order $1/m$.

Unlike the situation in bottomonium, corrections of order $1/m^2$ are large in charmonium. A manifestation of substantial $1/m^2$ effects is the relatively large observed splitting of 117 MeV between $\eta_c(1S)$ and J/ψ, driven by an effective coupling strength ($\alpha_s^{\rm eff}/m^2$ with $\alpha_s^{\rm eff} = 0.3$ in the phenomenological $\delta V_{\rm spin}$ of Eq. (7.6)) that is an order of magnitude larger than for bottomonium.

7.2.2 Extraction of the charm and bottom quark mass

To determine values for the quark masses at order $1/m$ a redefinition of the PS mass is required:

$$m_{\widehat{\rm PS}}(\mu_f, \mu_f') \equiv m_{\rm PS}(\mu_f) - \frac{1}{8m} C_F C_A \alpha_s^2(\overline{m})\, \mu_f'^2 \,. \tag{7.8}$$

The $1/m$ term stems from an analogous calculation as in the static case. The renormalization scale μ that appears in the coupling has again been identified with $\overline{m}$. We determine $m_{\widehat{\rm PS}}(\mu_f, \mu_f')$ for the b- and c-quark by fitting to the empirical $\Upsilon(2S)$ and $h_c(1P)$ energies, respectively, and convert these values numerically to $m_{\widehat{\rm PS}}(\overline{m}, \overline{m})$. This leads in a second step to the $1/m$-improved $\overline{\rm MS}$ values $\overline{m}_b = 4.18$ GeV for the bottom quark and $\overline{m}_c = 1.28$ GeV for the charm quark. In Table 7.1 the quark masses in the $\overline{\rm MS}$ scheme found in our approach are summarized and compared to values given by the Particle Data Group [65]. We have performed error estimates for the quark masses, reflecting uncertainties in the potentials (static and order $1/m$). Additional uncertainties are included from our specific choice of matching to the empirical $\Upsilon(2S)$ and $h_c(1P)$ energies. The errors at order $1/m$ have increased in comparison to those for the static case since they incorporate in addition the error band from $V^{(1)}$. The error estimates

$\overline{\rm MS}$ masses [GeV]			
	Static	Static + $\mathcal{O}(1/m)$	PDG 2010
Bottom quark	4.20 ± 0.04	$4.18^{+0.05}_{-0.04}$	$4.19^{+0.18}_{-0.06}$
Charm quark	1.23 ± 0.04	$1.28^{+0.07}_{-0.06}$	$1.27^{+0.07}_{-0.09}$

Table 7.1: Comparison of quark masses obtained in our approach (leading order plus order $1/m$ corrections) with the values listed by the Particle Data Group (PDG) [65]. See text for details concerning error estimates.

at order $1/m$ do not include possible further uncertainties appearing at order $1/m^2$.

7.3 Implications from new lattice QCD results

7.3.1 Charmonium spectroscopy

Finally, we discuss the charmonium spectrum below the $\mathrm{D\overline{D}}$ threshold that follows from the matched potentials based on the new lattice QCD results for charmonium (see Chapter 6). We focus on the 1S and 2S states which are not influenced by the tensor and spin-orbit interactions. The Schrödinger equation for these states,

$$\left[-\frac{\vec{\nabla}^2}{m} + 2m_{\widehat{\mathrm{PS}}}(\mu_C) + V_C(r) + \vec{S}_1 \cdot \vec{S}_2 \; V_S(r) - E \right] \psi(\vec{r}) = 0 \,, \tag{7.9}$$

involves a single free parameter $m_{\widehat{\mathrm{PS}}}(\mu_C)$, the ($\mu_C$-dependent) charm-quark mass in the potential-subtracted (PS) scheme. In order to make the PS scheme applicable here, we extend it by including the $1/m$ term[2]:

$$m_{\widehat{\mathrm{PS}}}(\mu_C) = m_{\mathrm{pole}} + \frac{1}{2} \int\limits_{q<\mu_C} \frac{d^3q}{(2\pi)^3} \left[\tilde{V}^{(0)}(q) + \frac{\tilde{V}^{(1)}(q)}{m/2} \right]. \tag{7.10}$$

Replacing the operator $\vec{S}_1 \cdot \vec{S}_2$ by its eigenvalues, $-3/4$ for the spin singlet and $1/4$ for the spin triplet, the Schrödinger equation (7.9) is solved numerically. The spin-spin potential $V_S(r)$ can be included in two different ways. In the first case it is treated in first-order perturbation theory, in the second case it is fully included in the Schrödinger equation. Due to the singular behavior of $V_S(r) \sim r^{-2.8}$ for $r \to 0$ (according to our construction) the wave functions diverge (mildly) in the latter case for very small values of r. In this case we solve the radial Schrödinger equation numerically for $r > 0.003$ fm and convince ourselves that the physical results are not affected by contributions coming from shorter distances. The results of the two alternative treatments of the spin-spin potential agree within 12 MeV (see Table 7.2). The calculated mass splittings between singlet and triplet states are in good agreement with experimental results for both 1S and 2S charmonia.

The single free parameter $m_{\widehat{\mathrm{PS}}}(\mu_C)$ is chosen such that the spin-weighted average of the 1S states agrees with its experimental value [65]. For the excited 2S states our approach predicts masses for $\eta_c(2\mathrm{S})$ and $\psi(2\mathrm{S})$ that are slightly too large (see Fig. 7.6). However, these states are close to the $\mathrm{D\overline{D}}$ threshold. Going beyond this threshold requires a complex (energy-dependent) $\mathrm{c\bar{c}}$ potential or an explicit treatment of coupled channels. While the imaginary part starts at the

[2]The PS mass $m_{\widehat{\mathrm{PS}}}(\mu)$ as defined here is equivalent with $m_{\widehat{\mathrm{PS}}}(\mu,\mu)$ of the previous section.

	Case 1	Case 2	Experiment [65]
1S mass splitting [MeV]	117 ± 6	105 ± 6	116.6 ± 1.2
2S mass splitting [MeV]	56 ± 3	46 ± 3	49 ± 4

Table 7.2: Predicted mass splittings of charmonium 1S and 2S multiplets in comparison with experimental data. Case 1: spin-spin potential treated in first-order perturbation theory. Case 2: spin-spin potential fully included in the Schrödinger equation.

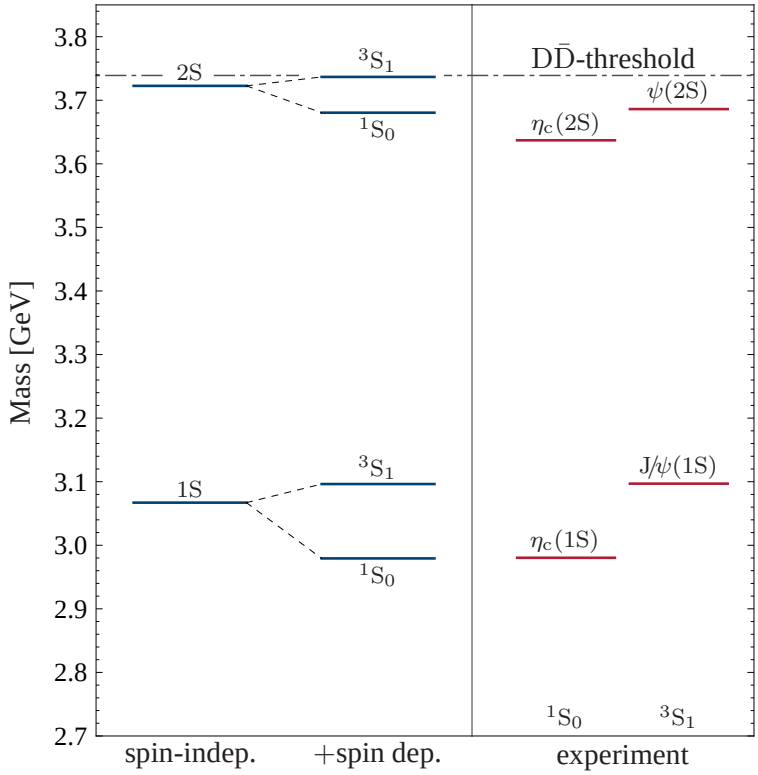

Figure 7.6: Predicted masses of charmonium 1S and 2S states in comparison with experimental data [65]. The results in the first column are based on the spin-independent potential only. The effects of the spin-spin potential, treated in first-order perturbation theory, are added in the second column.

opening of the $D\overline{D}$ channel, the corresponding dispersive real part induces an attractive shift of the 2S states. In second-order perturbation theory this shift is proportional to the squared $c\overline{c} \to D\overline{D}$ transition matrix element.

The predicted size of the hyperfine splittings is quite sensitive to the value of the mass m in the denominator of Eq. (6.14). For example, choosing $m = 1.5$ GeV instead of the kinetic quark mass $m_Q = (1.74 \pm 0.03)$ GeV [56] would give rise to a 1S mass splitting that is about 20% too large. This is in contrast

to variations of the matching position r_m and the infrared cutoff μ_S, which affect the hyperfine splittings only marginally.

The spin-spin potential, as constructed in Chapter 6, produces a non vanishing but small splitting between the 1P singlet and triplet states, namely $\mathrm{h_c}(1\mathrm{P})$ and $\chi_{\mathrm{cj}}(1\mathrm{P})$, unlike the δ-function spin-spin potential. In first-order perturbation theory the effect amounts to a mass difference of (8.2 ± 0.5) MeV. The full inclusion of the spin-spin potential $V_S(r)$ in the Schrödinger equation gives rise to a slightly larger mass splitting of (8.3 ± 0.5) MeV.

7.3.2 The charm-quark mass

The value of the mass parameter $m_{\widehat{\mathrm{PS}}}(\mu_C)$, determined in our approach by fitting to empirical charmonium spectra, can be translated as before into alternative schemes for quark masses. The PS mass $m_{\widehat{\mathrm{PS}}}(\mu_C)$ is again first converted to the pole mass and in a second step mapped onto the $\overline{\mathrm{MS}}$ mass $\overline{m}_c \equiv m_{\overline{\mathrm{MS}}}(m_{\overline{\mathrm{MS}}})$. Applying the same method as before, we find for the charm-quark mass in the $\overline{\mathrm{MS}}$ scheme

$$\overline{m}_c = (1.21 \pm 0.04)\ \mathrm{GeV}. \tag{7.11}$$

The error reflects combined uncertainties in the lattice potentials, in the input value of the strong coupling $\alpha_s(q)$, and from the matching to the empirical states.

7.3.3 Extension to bottomonium

Until now, the bottomonium spin-spin potential has not been studied within the new lattice QCD approach based on NBS amplitudes. An extrapolation of the spin-spin potential from charmonium to bottomonium can be done by simply assuming a $1/m^2$ dependence of the lattice potential and allowing for variations of the mass parameter m. In the perturbative part of the potential we account furthermore for a modified running of $\alpha_s(q)$ due to four massless flavors and use as before $\alpha_s(4.2\ \mathrm{GeV}) = 0.226 \pm 0.003$ as an input for bottomonium. The empirical mass splitting of (69 ± 3) MeV [65] between $\eta_{\mathrm{b}}(1\mathrm{S})$ and $\Upsilon(1\mathrm{S})$ can be reproduced either for a kinetic bottom-quark mass $m = 4.7$ GeV (with the spin-spin potential treated in first-order perturbation theory), or with $m = 4.3$ GeV (if the spin-spin potential is fully included in the Schrödinger equation).

8 Summary

Improved bottomonium and charmonium potentials have been derived in this work at leading order (static potential) and at order $1/m$ by systematically matching perturbative results to accurate lattice QCD data at an intermediate distance scale, $r = 0.14$ fm. By defining the perturbative potentials via a restricted Fourier transformation this matching has been made possible. The subthreshold bottomonium spectrum at order $1/m$, derived from a Schrödinger equation, agrees well with the experimental findings. As expected, the $1/m$-effects are far more pronounced for charmonium and higher-order corrections are needed in order to reproduce the experimental spectrum.

A single constant, the heavy-quark mass in the potential-subtracted scheme, is adjusted to reproduce the $\Upsilon(2S)$ mass (bottomonium case) and $h_c(1P)$ mass (charmonium case). The value of this mass can be translated to the $\overline{\text{MS}}$ scheme and agrees well with the c- and b-quark mass listed by the Particle Data Group.

Taking into account the running of α_s also at order $1/m^2$, we constructed perturbative spin-dependent potentials and found good agreement with lattice QCD for the spin-orbit and tensor potential.

We found, in addition, that the new central quark-antiquark potential based on NBS amplitudes (Chapter 6) agrees within errors with the static-plus-$1/m$ potential from the Chapters 3 and 4. The related matched spin-spin potential for charmonium produces hyperfine splittings for the S-wave charmonium states that are in good agreement with experiment. A slightly smaller $\overline{\text{MS}}$ mass for the charm quark is found in this approach.

Appendix

A.1 The beta function in QCD

The QCD β-function, the function which specifies the scale dependence of the strong coupling, is defined as

$$\frac{\partial \alpha_s(\mu^2)}{\partial \ln \mu^2} = \beta(\alpha_s) = -\frac{\alpha_s^2}{4\pi}\beta_0 - \frac{\alpha_s^3}{(4\pi)^2}\beta_1 - \frac{\alpha_s^4}{(4\pi)^3}\beta_2 - \frac{\alpha_s^5}{(4\pi)^4}\beta_3 + \mathcal{O}(\alpha_s^6)\,. \quad \text{(A.1)}$$

The coefficients β_n have been calculated at four-loop order [66]. They have the following form for $N = 3$ colors in the $\overline{\text{MS}}$-scheme:

$$\beta_0 = 11 - \frac{2}{3}n_f\,, \quad \text{(A.2a)}$$

$$\beta_1 = 102 - \frac{38}{3}n_f\,, \quad \text{(A.2b)}$$

$$\beta_2 = \frac{2857}{2} - \frac{5033}{18}n_f + \frac{325}{54}n_f^2\,, \quad \text{(A.2c)}$$

$$\beta_3 = \left(\frac{149753}{6} + 3564\,\zeta(3)\right) - \left(\frac{1078361}{162} + \frac{6508}{27}\,\zeta(3)\right)n_f + \left(\frac{50065}{162} + \frac{6472}{81}\,\zeta(3)\right)n_f^2 + \frac{1093}{729}\,n_f^3\,, \quad \text{(A.2d)}$$

where n_f is the number of active quark flavors and $\zeta(s)$ represents the Riemann zeta function

$$\zeta(s) \equiv \sum_{k=1}^{\infty} \frac{1}{k^s}\,. \quad \text{(A.3)}$$

Only at one-loop order exists an analytical formula for the running of α_s. It is obtained easily from the leading term in Eq. (A.1) and reads:

$$\alpha_s(\mu) = \frac{\alpha_s(\mu_0)}{1 + \frac{\beta_0}{4\pi}\,\alpha_s(\mu_0)\ln\frac{\mu^2}{\mu_0^2}}\,. \quad \text{(A.4)}$$

Beyond leading order one can derive an expansion that approximates the running of $\alpha_s(\mu)$ to high accuracy. After introducing $a(\mu) = \alpha_s(\mu)/\pi$ and performing an

integration one gets:

$$\begin{aligned}\ln\frac{\mu^2}{\Lambda^2} &= \int\frac{\pi}{\beta(a)}\,da \\ &= \frac{4}{\beta_0 a}+\frac{\beta_1}{\beta_0^2}\ln a+\left(\frac{\beta_2}{4\beta_0^2}-\frac{\beta_1^2}{4\beta_0^3}\right)a \\ &\quad+\left(\frac{\beta_3}{32\beta_0^2}-\frac{\beta_1\beta_2}{16\beta_0^3}+\frac{\beta_1^3}{32\beta_0^4}\right)a^2+\mathcal{O}(a^3)+C\,. \end{aligned} \tag{A.5}$$

The parameter Λ is identical to the scale μ where $\alpha_s(\mu)$ diverges to infinity. The conventional definition

$$C=\frac{\beta_1}{\beta_0^2}\ln(\beta_0/4)\,, \tag{A.6}$$

is used for the arbitrary constant C. An iterative inversion of Eq. (A.5) gives the four-loop approximation with $L=\ln(\mu^2/\Lambda^2)$:

$$\begin{aligned}a(\mu) &= \frac{4}{\beta_0 L}-\frac{4\beta_1\ln L}{\beta_0^3 L^2}+\frac{4}{\beta_0^5 L^3}\Big[\beta_0\beta_2+\beta_1^2(\ln^2 L-\ln L-1)\Big] \\ &\quad+\frac{2}{\beta_0^7 L^4}\Big[\beta_0^2\beta_3-6\beta_0\beta_1\beta_2\ln L+\beta_1^3(-2\ln^3 L+5\ln^2 L+4\ln L-1)\Big] \\ &\quad+\mathcal{O}(1/L^5)\,, \end{aligned} \tag{A.7}$$

in agreement with the literature [67].

Alternatively, the scale dependence of the strong coupling can be approximated by a power series expansion about a fixed scale μ_0:

$$\begin{aligned}\alpha_s(\mu) = \alpha_s(\mu_0)\Bigg[1 &- \frac{\alpha_s(\mu_0)}{4\pi}\beta_0\,\ell+\left(\frac{\alpha_s(\mu_0)}{4\pi}\right)^2(\beta_0^2\,\ell-\beta_1)\,\ell \\ &+\left(\frac{\alpha_s(\mu_0)}{4\pi}\right)^3\left(-\beta_0^3\,\ell^2+\frac{5}{2}\beta_0\beta_1\,\ell-\beta_2\right)\ell \\ &+\left(\frac{\alpha_s(\mu_0)}{4\pi}\right)^4\left(\beta_0^4\,\ell^3-\frac{13}{3}\beta_0^2\beta_1\,\ell^2+3\beta_0\beta_2\,\ell+\frac{3}{2}\beta_1^2\,\ell-\beta_3\right)\ell \\ &+\mathcal{O}\left(\alpha_s^5\right)\Bigg], \end{aligned} \tag{A.8}$$

with $\ell=\ln(\mu^2/\mu_0^2)$. This expansion is derived from Eq. (A.7), after eliminating the parameter Λ. The approximation is only valid around the scale μ_0, as shown in Fig. A.1. This is in contrast to Eq. (A.7), that gives a good approximation for $\alpha_s(\mu)$ over many orders of magnitude.

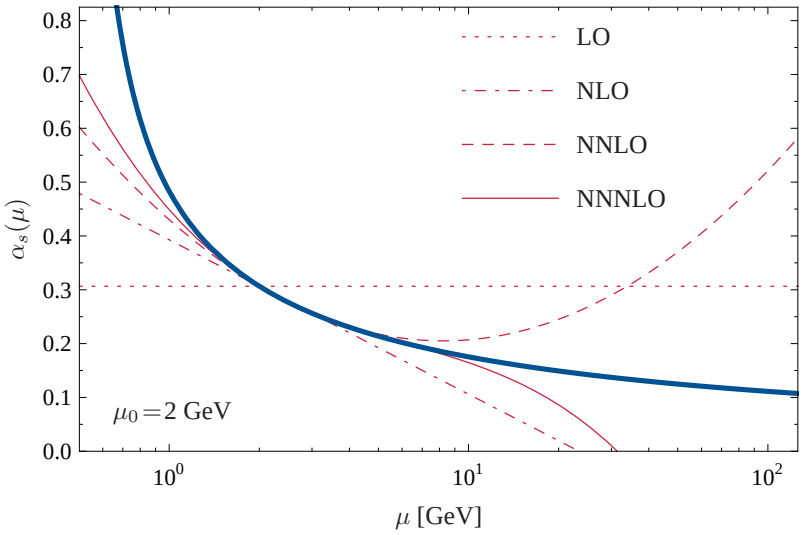

Figure A.1: Power series expansion of $\alpha_s(\mu)$ according to Eq. (A.8). Different orders in $\alpha_s(\mu_0)$ are shown in comparison with the full four-loop running (thick line). The expansion has been performed at $\mu_0 = 2$ GeV and with $n_f = 4$. Note that the sign of $\alpha_s(q \to \infty)$ changes order by order.

A.2 Flavor thresholds

The beta function in QCD depends on the number of quark flavors and thus also the resulting coupling $\alpha_s^{(n_f)}(\mu)$. For clearness, the superscript (n_f) is added to α_s in this section. To allow for an accurate definition of the charmonium and bottomonium potentials, we need to know $\alpha_s^{(n_f)}(\mu)$ for $n_f = 3$ (charmonium case) and $n_f = 4$ (bottomonium case) as precisely as possible.

The running of the strong coupling by itself is obtained from the beta function (see previous section), but in addition a starting point has to be known for the different values of n_f. For $n_f = 5$ we use (see Ref. [29]),

$$\alpha_s^{(5)}(m_Z = 91.1876 \text{ GeV}) = 0.1184 \pm 0.0007\,, \tag{A.9}$$

an average value that is based on many different measurements of α_s and also on lattice QCD. The connection between $\alpha_s^{(n_f)}(\mu)$ for different numbers of quark flavors can be accomplished by making use of the framework of effective field theories. One considers an idealized theory of QCD with one heavy-quark flavor (with mass m_h) and $n_l = n_f - 1$ massless flavors and constructs an effective theory with n_l flavors. The two theories are matched around the threshold of the heavy quark. If four-loop running is implemented, a consistent matching has to be done at three-loop order.

The matching condition up to three-loop order is derived in Ref. [67] and reads in the $\overline{\text{MS}}$-scheme for an arbitrary scale μ not to far from the mass of the

heavy quark m_h:

$$\frac{\alpha_s^{(n_l)}(\mu)}{\pi} = a - a^2\,\frac{l_h}{6} + a^3\left[\frac{l_h^2}{36} - \frac{19}{24}l_h + \frac{11}{72}\right] + a^4\Bigg[- \frac{l_h^3}{216} - \frac{131}{576}l_h^2 + \frac{l_h}{1728}(-6793+281n_l) + \frac{564731}{124416} - \frac{82043}{27648}\zeta(3) - \frac{2633}{31104}n_l\Bigg] + \mathcal{O}(a^5)\,, \tag{A.10}$$

where $a = \alpha_s^{(n_f)}(\mu)/\pi$ and $l_h = 2\ln[\mu/m_h(m_h)]$.

After using four-loop running to translate $\alpha_s^{(5)}(m_Z = 91.1876\text{ GeV}) = 0.1184 \pm 0.0007$ to $\alpha_s^{(5)}(4.2\text{ GeV})$, one finds with Eq. (A.10) for the strong coupling in a theory with four flavors:

$$\alpha_s^{(4)}(4.2\text{ GeV}) = 0.226 \pm 0.003\,. \tag{A.11}$$

To obtain $\alpha_s^{(3)}(\mu)$, we run this value further down to $\alpha_s^{(4)}(1.25\text{ GeV})$ (with $n_f = 4$) and apply Eq. (A.10) a second time. One finds:

$$\alpha_s^{(3)}(1.25\text{ GeV}) = 0.406 \pm 0.010\,. \tag{A.12}$$

This result can be used as an input value for the running of a theory with three flavors.

A.3 One-gluon exchange

A simple method to account for spin-dependent effects in potential models is to consider one-gluon exchange, which is analogous to the Breit-Fermi interaction in QED. Even though the full QCD potential at order $1/m^2$ has been obtained in pNRQCD (see Section 5.1), one-gluon exchange can still be used to approximate the spin dependency for phenomenological applications. It played an important role in understanding quarkonium spectroscopy and we include it for orientation in Section 7.2.

The following color contact interaction, giving rise for example for the splitting between J/ψ and η_c(1S), is found in one-gluon exchange:

$$V_{\text{contact}} = \frac{32\pi\alpha_s}{9m^2}\,(\vec{S}_1 \cdot \vec{S}_2)\,\delta^{(3)}(\vec{r}\,)\,. \tag{A.13}$$

It corresponds to $V_{S^2}^{(1,1)}$ (in the language of Section 5.1) taken at leading order in perturbation theory.

The color tensor interaction, corresponding to $V_{\vec{S}_{12}}^{(1,1)}(r)$ at leading order in perturbation theory,

$$V_{\text{tensor}} = \frac{4\alpha_s}{m^2}\left(\frac{(\vec{S}_1\cdot\vec{r}\,)(\vec{S}_2\cdot\vec{r}\,)}{r^5} - \frac{\vec{S}_1\cdot\vec{S}_2}{3\,r^3}\right), \tag{A.14}$$

contributes to the splitting of the spin-triplet multiplets.

The spin-orbit term is the final spin-dependent interaction found in one-gluon exchange:

$$V_{\text{spin-orbit}} = \frac{2\alpha_s}{m^2}\left(\frac{\vec{L}\cdot\vec{S}_1 + \vec{L}\cdot\vec{S}_2}{r^3}\right). \tag{A.15}$$

It arises from a combination of the color-magnetic piece and a relativistic correction, the Thomas-precession term. The spin-orbit term agrees with the effective-field-theory result at order $1/m^2$ when $V_{LS}^{(2,0)}(r)$, $V_{LS}^{(0,2)}(r)$, $V_{L_1S_2}^{(1,1)}(r)$ and $V_{L_2S_1}^{(1,1)}(r)$ are taken at leading order in perturbation theory.

List of figures

List of tables

References

[1] **Quarkonium Working Group** Collaboration, N. Brambilla *et al.*, "Heavy quarkonium physics," arXiv:hep-ph/0412158.

[2] N. Brambilla, S. Eidelman, B. K. Heltsley, R. Vogt, G. T. Bodwin, *et al.*, "Heavy quarkonium: progress, puzzles, and opportunities," *Eur. Phys. J.* **C71** (2011) 1534.

[3] T. Appelquist and H. D. Politzer, "Heavy quarks and e^+e^- annihilation," *Phys. Rev. Lett.* **34** (1975) 43.

[4] W. E. Caswell and G. P. Lepage, "Effective Lagrangians for bound state problems in QED, QCD, and other field theories," *Phys. Lett.* **B167** (1986) 437.

[5] G. T. Bodwin, E. Braaten, and G. P. Lepage, "Rigorous QCD analysis of inclusive annihilation and production of heavy quarkonium," *Phys. Rev.* **D51** (1995) 1125; erratum *ibid.* **D55** (1997) 5853.

[6] A. V. Manohar, "Heavy quark effective theory and nonrelativistic QCD Lagrangian to order α_s/m^3," *Phys. Rev.* **D56** (1997) 230.

[7] A. Pineda and J. Soto, "Matching at one loop for the four-quark operators in NRQCD," *Phys. Rev.* **D58** (1998) 114011.

[8] A. Pineda and J. Soto, "Effective field theory for ultrasoft momenta in NRQCD and NRQED," *Nucl. Phys. B (Proc. Suppl.)* **64** (1998) 428.

[9] N. Brambilla, A. Pineda, J. Soto, and A. Vairo, "Potential NRQCD: an effective theory for heavy quarkonium," *Nucl. Phys.* **B566** (2000) 275.

[10] A. S. Kronfeld, "Perturbative pole mass in QCD," *Phys. Rev.* **D58** (1998) 051501(R).

[11] A. H. Hoang, "Heavy quarkonium dynamics," in *At the Frontier of Particle Physics: Handbook of QCD*, edited by M. Shifman (World Scientific, Singapore 2002) Vol. 4 p. 2215.

[12] M. Beneke, "A quark mass definition adequate for threshold problems," *Phys. Lett.* **B434** (1998) 115.

[13] A. H. Hoang, M. C. Smith, T. Stelzer, and S. Willenbrock, "Quarkonia and the pole mass," *Phys. Rev.* **D59** (1999) 114014.

[14] I. Bigi, M. Shifman, N. Uraltsev, and A. Vainshtein, "High power n of m_b in b-flavored widths and $n = 5 \to \infty$ limit," *Phys. Rev.* **D56** (1997) 4017.

[15] A. H. Hoang, Z. Ligeti, and A. V. Manohar, "B decay and the Υ mass," *Phys. Rev. Lett.* **82** (1999) 277.

[16] A. Pineda, "Determination of the bottom quark mass from the $\Upsilon(1S)$ system," *JHEP* **0106** (2001) 022.

[17] G. Bali and K. Schilling, "Static quark-antiquark potential: Scaling behavior and finite size effects in SU(3) lattice gauge theory," *Phys. Rev.* **D46** (1992) 2636.

[18] G. S. Bali *et al.*, "Static potentials and glueball masses from QCD simulations with Wilson sea quarks," *Phys. Rev.* **D62** (2000) 054503.

[19] M. Peter, "Static quark-antiquark potential in QCD to three loops," *Phys. Rev. Lett.* **78** (1997) 602.

[20] M. Peter, "The static potential in QCD – a full two-loop calculation," *Nucl. Phys.* **B501** (1997) 471.

[21] Y. Schröder, "The static potential in QCD to two loops," *Phys. Lett.* **B447** (1999) 321.

[22] N. Brambilla, A. Pineda, J. Soto, and A. Vairo, "Infrared behavior of the static potential in perturbative QCD," *Phys. Rev.* **D60** (1999) 091502.

[23] A. V. Smirnov, V. A. Smirnov, and M. Steinhauser, "Three-loop static potential," *Phys. Rev. Lett.* **104** (2010) 112002.

[24] C. Anzai, Y. Kiyo, and Y. Sumino, "Static QCD potential at three-loop order," *Phys. Rev. Lett.* **104** (2010) 112003.

[25] U. Aglietti and Z. Ligeti, "Renormalons and the quark potential," *Phys. Lett.* **B364** (1995) 75.

[26] M. Beneke, "Renormalons," *Phys. Rept.* **317** (1999) 1.

[27] A. Pineda, "The static potential: lattice versus perturbation theory in a renormalon based approach," *J. Phys.* **G29** (2003) 371.

[28] A. Laschka, N. Kaiser, and W. Weise, "Quark-antiquark potential to order $1/m$ and heavy quark masses," *Phys. Rev.* **D83** (2011) 094002.

[29] S. Bethke, "The 2009 world average of α_s," *Eur. Phys. J.* **C64** (2009) 689.

[30] S. Necco and R. Sommer, "The $N_f = 0$ heavy quark potential from short to intermediate distances," *Nucl. Phys.* **B622** (2002) 328.

[31] N. Brambilla, X. Garcia i Tormo, J. Soto, and A. Vairo, "Precision determination of $r_0\Lambda_{\overline{\rm MS}}$ from the QCD static energy," *Phys. Rev. Lett.* **105** (2010) 212001.

[32] N. Brambilla, A. Pineda, J. Soto, and A. Vairo, "QCD potential at $O(1/m)$," *Phys. Rev.* **D63** (2000) 014023.

[33] K. Melnikov and A. Yelkhovsky, "Top quark production at threshold with $\mathcal{O}(\alpha_s^2)$ accuracy," *Nucl. Phys.* **B528** (1998) 59.

[34] A. H. Hoang, "Bottom quark mass from Υ mesons," *Phys. Rev.* **D59** (1998) 014039.

[35] Y. Koma, M. Koma, and H. Wittig, "Nonperturbative determination of the QCD potential at $O(1/m)$," *Phys. Rev. Lett.* **97** (2006) 122003.

[36] M. Lüscher and P. Weisz, "Locality and exponential error reduction in numerical lattice gauge theory," *JHEP* **0109** (2001) 010.

[37] M. Lüscher and P. Weisz, "Quark confinement and the bosonic string," *JHEP* **0207** (2002) 049.

[38] M. Koma, Y. Koma, and H. Wittig, "Determination of the spin-dependent potentials with the multi-level algorithm," *PoS* **LAT2005** (2005) 216.

[39] Y. Koma and M. Koma, "Spin-dependent potentials from lattice QCD," *Nucl. Phys.* **B769** (2007) 79.

[40] M. Koma, Y. Koma, and H. Wittig, "Determination of the relativistic corrections to the static inter-quark potential from lattice QCD," *PoS* **Confinement8** (2008) 105.

[41] G. Perez-Nadal and J. Soto, "Effective-string-theory constraints on the long-distance behavior of the subleading potentials," *Phys. Rev.* **D79** (2009) 114002.

[42] A. Pineda and A. Vairo, "The QCD potential at $\mathcal{O}(1/m^2)$: Complete spin-dependent and spin-independent result," *Phys. Rev.* **D63** (2001) 054007; erratum *ibid.* **D64** (2001) 039902(E).

[43] P. de Forcrand and J. D. Stack, "Spin-dependent potentials in SU(3) lattice gauge theory," *Phys. Rev. Lett.* **55** (1985) 1254.

[44] C. Michael, "Long-range spin-orbit potential," *Phys. Rev. Lett.* **56** (1986) 1219.

[45] M. Campostrini, K. Moriarty, and C. Rebbi, "Monte Carlo calculation of the spin-dependent potentials for heavy-quark spectroscopy," *Phys. Rev. Lett.* **57** (1986) 44.

[46] K. D. Born, E. Laermann, T. F. Walsh, and P. M. Zerwas, "Spin dependence of the heavy-quark potential: a QCD lattice analysis," *Phys. Lett.* **B329** (1994) 332.

[47] G. S. Bali, K. Schilling, and A. Wachter, "Complete $O(v^2)$ corrections to the static interquark potential from SU(3) gauge theory," *Phys. Rev.* **D56** (1997) 2566.

[48] Y. Koma and M. Koma, "Scaling study of the relativistic corrections to the static potential," *PoS* **LAT2009** (2009) 122.

[49] E. Eichten and F. Feinberg, "Spin-dependent forces in quantum chromodynamics," *Phys. Rev.* **D23** (1981) 2724.

[50] D. Gromes, "Relativistic corrections to the long-range quark antiquark potential, electric flux tubes, and area law," *Z. Phys.* **C22** (1984) 265.

[51] Y. Koma, M. Koma, and H. Wittig, "Relativistic corrections to the static potential at $O(1/m)$ and $O(1/m^2)$," *PoS* **LAT2007** (2007) 111.

[52] A. Barchielli, E. Montaldi, and G. M. Prosperi, "On a systematic derivation of the quark-antiquark potential," *Nucl. Phys.* **B296** (1988) 625; erratum *ibid.* **B303** (1988) 752.

[53] A. Barchielli, N. Brambilla, and G. M. Prosperi, "Relativistic corrections to the quark-antiquark potential and the quarkonium spectrum," *Nuovo Cim.* **A103** (1990) 59.

[54] B. A. Kniehl, A. A. Penin, V. A. Smirnov, and M. Steinhauser, "Potential NRQCD and heavy-quarkonium spectrum at next-to-next-to-next-to-leading order," *Nucl. Phys.* **B635** (2002) 357.

[55] T. Kawanai and S. Sasaki, "Interquark potential with finite quark mass from lattice QCD," *Phys. Rev. Lett.* **107** (2011) 091601.

[56] T. Kawanai and S. Sasaki, "Charmonium potential from full lattice QCD," *Phys. Rev.* **D85** (2012) 091503(R).

[57] T. Barnes, S. Godfrey, and E. S. Swanson, "Higher charmonia," *Phys. Rev.* **D72** (2005) 054026.

[58] A. Laschka, N. Kaiser, and W. Weise, "Charmonium potentials: Matching perturbative and lattice QCD," *Phys. Lett.* **B715** (2012) 190.

[59] N. Brambilla, A. Pineda, J. Soto, and A. Vairo, "Effective field theories for heavy quarkonium," *Rev. Mod. Phys.* **77** (2005) 1423.

[60] S. Dobbs, Z. Metreveli, A. Tomaradze, T. Xiao, and K. K. Seth, "Observation of the $\eta_b(2S)$ meson in $\Upsilon(2S) \to \gamma\eta_b(2S)$, $\eta_b(2S) \to$ hadrons and confirmation of the $\eta_b(1S)$ meson," *Phys. Rev. Lett.* **109** (2012) 082001.

[61] R. Mizuk *et al.*, "Evidence for the $\eta_b(2S)$ and observation of $h_b(1P) \to \eta_b(1S)\gamma$ and $h_b(2P) \to \eta_b(1S)\gamma$," arXiv:1205.6351 [hep-ex].

[62] K. G. Chetyrkin and M. Steinhauser, "Short-distance mass of a heavy quark at order α_s^3," *Phys. Rev. Lett.* **83** (1999) 4001.

[63] K. G. Chetyrkin and M. Steinhauser, "The relation between the $\overline{\rm MS}$ and the on-shell quark mass at order α_s^3," *Nucl. Phys.* **B573** (2000) 617.

[64] K. Melnikov and T. v. Ritbergen, "The three-loop relation between the $\overline{\rm MS}$ and the pole quark masses," *Phys. Lett.* **B482** (2000) 99.

[65] **Particle Data Group** Collaboration, K. Nakamura *et al.*, "Review of particle physics," *J. Phys.* **G37** (2010) 075021.

[66] T. van Ritbergen, J. A. M. Vermaseren, and S. A. Larin, "The four-loop β-function in quantum chromodynamics," *Phys. Lett.* **B400** (1997) 379.

[67] K. G. Chetyrkin, B. A. Kniehl, and M. Steinhauser, "Strong coupling constant with flavor thresholds at four loops in the modified minimal-subtraction scheme," *Phys. Rev. Lett.* **79** (1997) 2184.

Acknowledgments

This project would not have been possible without the contribution of many people. In these final lines I want to show my gratitude to at least a few of them.

First of all I would like to thank Wolfram Weise for his guidance and for making this dissertation possible. He has always been available for discussions, suggestions and comments concerning my work. Furthermore, I am grateful to him for giving me the opportunity to participate in various workshops and conferences.

I would like to express my gratitude to Norbert Kaiser for his assistance with any kind of physical or mathematical questions.

I thank Nora Brambilla and Antonio Vairo for numerous useful discussions and helpful comments.

In addition, I want to thank all current and previous members of T39, especially Michael Altenbuchinger, Nino Bratovic, Matthias Drews, Maximilian Duell, Salvatore Fiorilla, Lisheng Geng, Philipp Hägler, Thomas Hell, Jeremy Holt, Kouji Kashiwa, Bertram Klein, Youngshin Kwon, Robert Lang, Bernhard Musch, Stefan Petschauer, Paul Springer and Corbinian Wellenhofer, for frequent discussions on various topics, the pleasant working atmosphere and for spare-time activities.

I would like to acknowledge the transferable skills training and the financial support of the TUM Graduate School.

Finally, I am truly indebted to my family and my friends for their continuous support.